Title

Integrated Spectrally-Selective Infrared Sensors based on RF MEMS

ISBN
9798290615202

Author
Huang, Johnny

Publication Date
2025-06-15

Peer reviewed|Thesis/dissertation

Integrated Spectrally-Selective Infrared Sensors based on RF MEMS

By

JOHNNY HUANG

THESIS

Submitted in partial satisfaction of the requirements for the degree of

MASTER OF SCIENCE

in

Electrical and Computer Engineering

in the

OFFICE OF GRADUATE STUDIES

of the

UNIVERSITY OF CALIFORNIA

DAVIS

Approved:

Juan Sebastian Gomez-Diaz, Chair

William Putnam

Omeed Momeni

Committee in Charge

2025

Contents

List of Figures

List of Tables

Abstract

Integrated Spectrally-Selective Infrared Sensors based on RF MEMS

Current standard methods for detection of head and neck cancer using biofluids consist of using mass spectrometry with bulky and expensive instruments. This thesis presents the realization of an existing bench top radio frequency (RF) system onto a printed circuit board (PCB), which aims to interface with an infrared (IR) detecting micro electromechanical system (MEMS) to perform IR spectroscopy and sensing, providing an inexpensive and portable alternative to existing IR spectroscopy and sensing technologies. Keysight's Advance Design System (ADS) was utilized to analyze a series of simulations to predict the validity of the system. Then, Altium was used to realize the RF system onto a PCB. To confirm the functionality of the designed PCB, a series of experiments that were conducted with the bench top RF system were replicated. These experimental results and the design process are presented to not only validate the functionality of the realized RF system onto a PCB, but also to contribute to the development of a miniaturized and portable system for IR spectroscopy and detecting.

Acknowledgments

I would like to thank the PhD members in the research lab, Zhixing Lin, Matthew Benson, and Melissa Gulseren for their assistance and support during my time as a graduate student working in the lab. I am extremely grateful for the help they have provided me, allowing me to accomplish the work presented.

I also want to express my gratitude to my professor, Juan Sebastian Gomez Diaz, for providing me this opportunity and the guidance needed to succeed. He has fostered a supportive and encouraging environment that I am very grateful for.

Chapter 1

Introduction

1.1 Fundamentals of IR Detecting MEMS

The increasing utilization of sensors in our everyday lives exemplifies the importance of miniaturized and cost-effective sensors that operate at room temperature. Here at UC Davis, at the Applied Micro/Nano Electromagnetics Research Laboratory, graduate PhD students have fabricated and characterized the performance of selective infrared (IR) micro electromechanical systems (MEMS) sensors. Thin films of material that absorb IR radiation are placed onto the surface of the MEMS, which converts the IR signal incoming onto the device to detectable electrical signals, as shown in Figure 1.1 below [1].

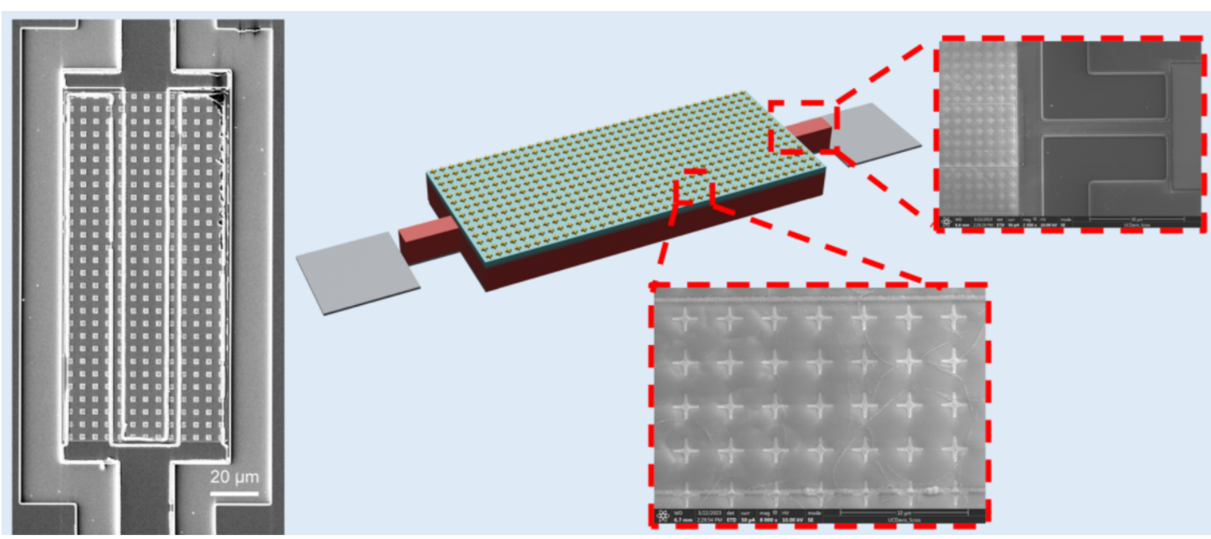

Figure 1.1: Detailed image of MEMS with IR absorbing material [2].

The MEMS is a piezoelectric resonator and is excited at a specific resonant frequency using a signal generator. When an IR signal is incident onto the MEMS, it heats up, leading to a resonant frequency shift due to the temperature coefficient of frequency (TCF) of the piezoelectric resonator [3, 4]. This frequency shift results in a shift in the magnitude and phase response, as depicted in Figure 1.2. The magnitude and phase variations caused by the frequency shift are directly correlated to the IR power and wavelength. The spectral response of the MEMS is displayed in Figure 1.3, where the responsivity of the MEMS is dependent on the incident wavelength of the IR signal. This allows us to detect both the power and wavelength of the IR signal incident upon the MEMS, while operating at room temperature.

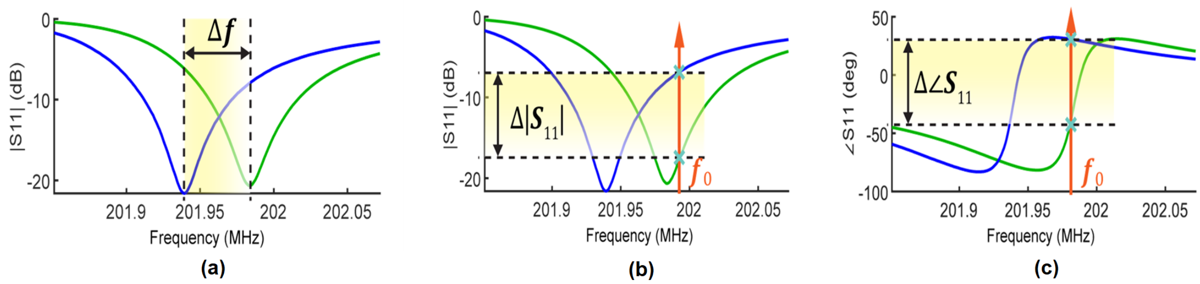

Figure 1.2: IR shift response of MEMS shown in Figure 1.1 vs. frequency, magnitude, and phase (a) Frequency shift (b) Magnitude shift due to shift in resonant frequency f_o (c) Phase shift due to shift in resonant frequency f_o [2].

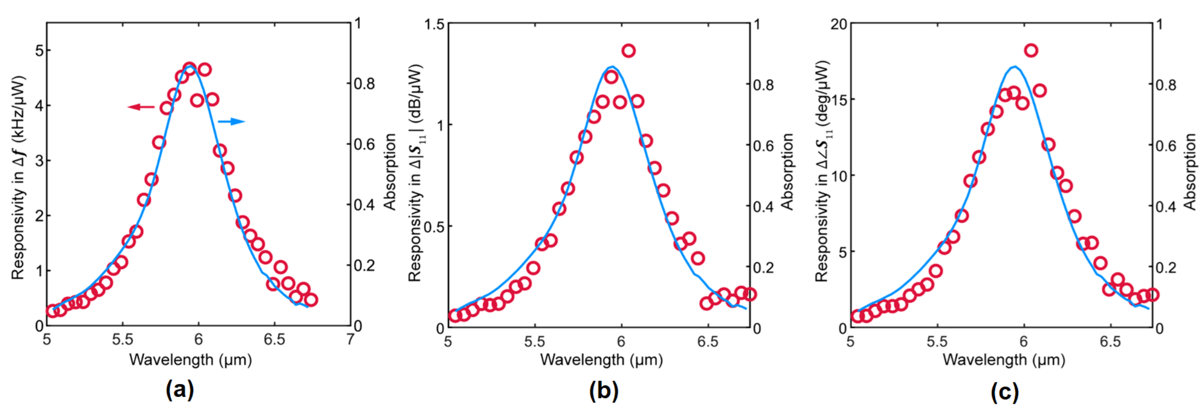

Figure 1.3: MEMS spectral response across different wavelengths (a) Responsivity of frequency shift (b) Responsivity of magnitude shift (c) Responsivity of phase shift [2].

IR detectors are used in a variety of applications in many different fields, such as studying stars, cancer or tumor detection, and thermal imaging [5]. The intended goal and focus of this thesis works towards developing the depicted device in Figure 1.4, which will be used to detect head and neck cancer via IR spectroscopy using the MEMS as the detector. With this device, users will be able to provide a blood or saliva sample, and the device will provide spectral information similar to common Fourier Transform Infrared spectroscopy (FTIR) tools. This will inform the users whether they should seek additional assistance from professional specialists. This device will provide a cheaper and portable alternative to traditional bulky, complex, and expensive FTIR instruments involved in analyzing biofluids. However, it should also be noted that the MEMS is not only limited to this specific application, since it functions as any traditional IR detectors.

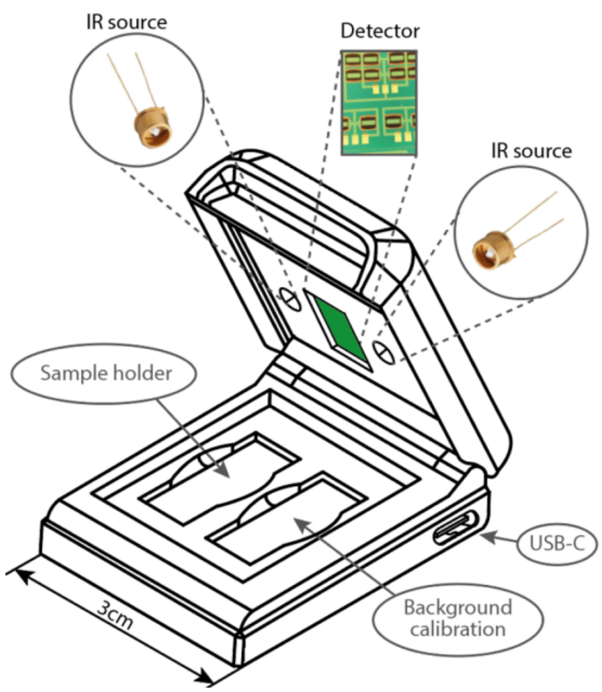

Figure 1.4: Overview of cancer detecting device.

1.2 Overview of RF System

The bench-top experimental set-up shown below in Figure 1.5 depicts the measurement configuration that we currently have in the lab. It consists of three sections: the infrared, microscope, and RF sections. The main function of the infrared section is to provide the IR signal and control the power of the IR signal that is incident onto the MEMS. The main function of the microscope section is to focus the IR signal and to provide a clear image to land the GSG probes onto the MEMS. The section of relevance for this thesis is the RF section, which will be realized by the PCB.

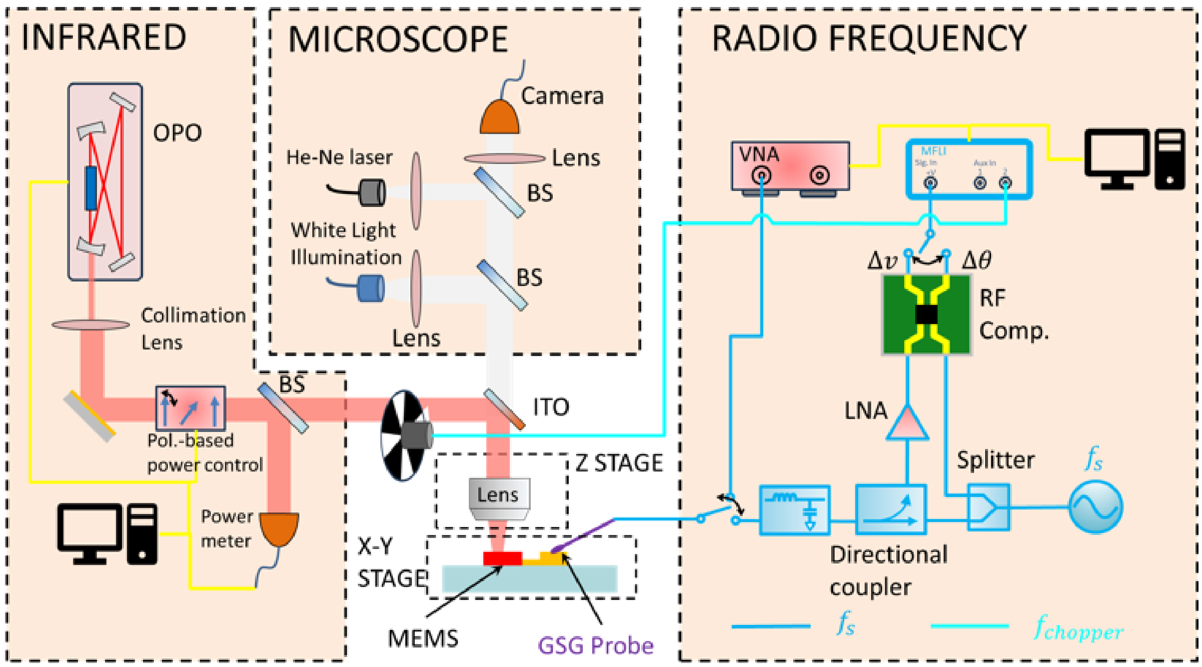

Figure 1.5: Block diagram of lab experimental set-up [2].

In the bench-top set-up, a signal generator is used to produce the reference signal, and excites the MEMS through a directional coupler. The reflected signal from the MEMS is measured using a GSG (Ground-signal-ground) probe and travels through an LC matching network that can be tunable using a mechanical varactor. The matching network is utilized to improve the responsivity of the MEMS sensor. The measured reflected signal then travels through the coupled port of the directional coupler and amplified using a low noise amplifier (LNA) before being transmitted into the input of the RF comparator. The directional coupler allows the excitatory signal to travel to the MEMS, while also being able to measure the reflected signal from the coupled port of the coupler. Due to a ∼20dB loss between the coupled port and the mainline, an LNA is used to amplify the reflected signal to a detectable level. The RF comparator takes both the reference and reflected signal as inputs, and outputs two DC voltages (one for magnitude and one for phase) that are proportional to the phase and magnitude difference between the reflected signal and the reference signal.

The RF comparator IC used is Analog Devices' AD8302; its general block diagram and the expected magnitude and phase output voltage plots are depicted in Figure 1.6.

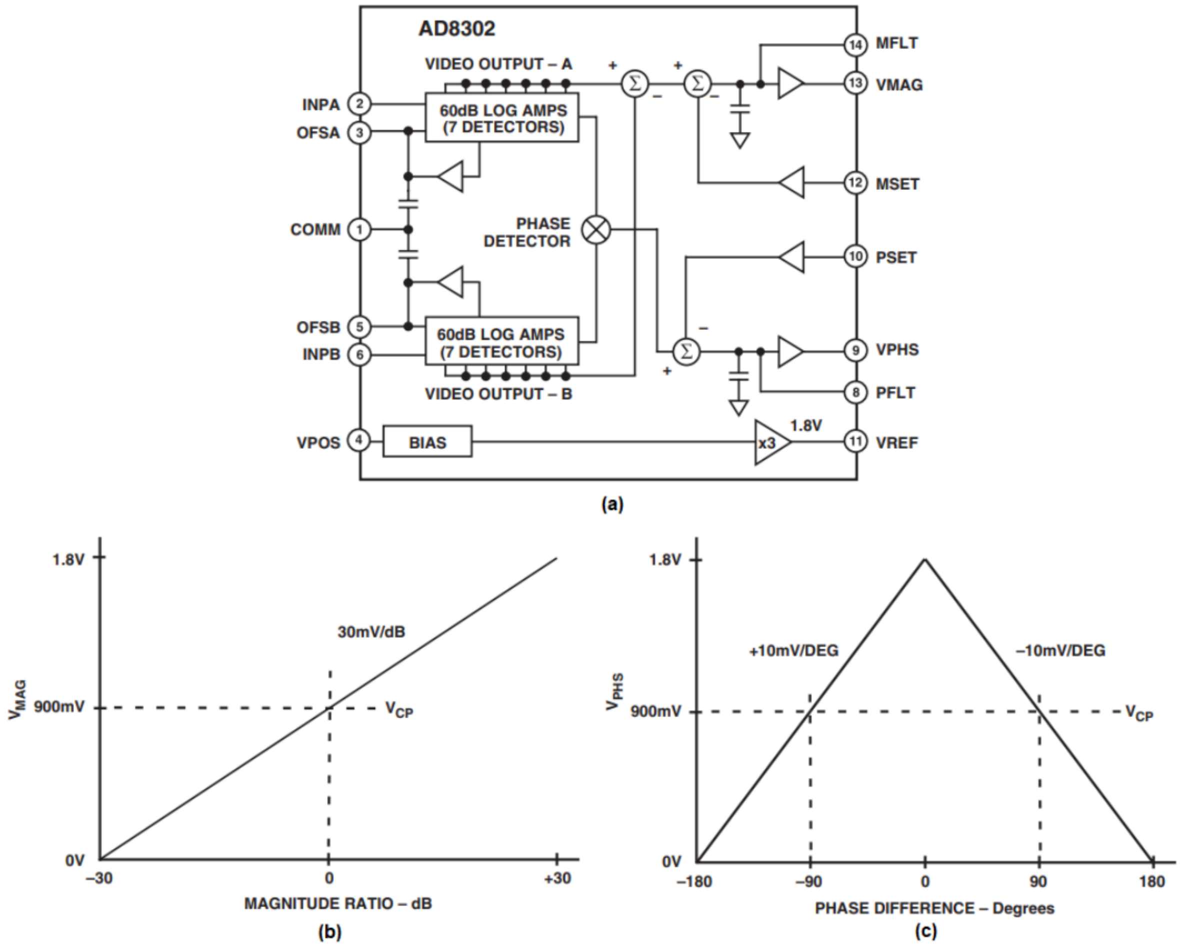

Figure 1.6: AD8302 schematic (a) and output voltage plots (b-c) [6].

Inside the RF comparator are two logarithmic amplifiers, one for each input, providing a large detectable measurement range of 60dB for the input signals. The general voltage output expression for a logarithmic amplifier output is [6]:

$$V_{out} \approx V_Y \log(\frac{V_{IN}}{V_X}) \tag{1.1}$$

Where V_Y is the slope of the transfer function and V_X is the intercept voltage defined as the point when the logarithm is 0 when $V_{IN} = V_X$. However, the AD8302 RF comparator takes the difference between the two identical logarithmic amplifiers in current domain, resulting in:

$$V_{MAG} = V_{SLOPE} \log(\frac{V_{INA}}{V_{INB}}) \tag{1.2}$$

$$V_{PHS} = V_{\Phi SLOPE}(\Phi V_{INA} - \Phi V_{INB}) \tag{1.3}$$

The incoming IR power is directly correlated to the magnitude and phase shift of the reflected signal from the MEMS, as depicted in Figure 1.2. Therefore, when the reference signal is compared to the reflected signal from the MEMS, it is observed from equations 1.2 and 1.3 that the output voltage for the magnitude and phase is directly proportional to the phase and magnitude shift caused by the incident IR signal onto the MEMS.

Chapter 2

ADS Simulations

2.1 MEMS Model & LC Matching Network

A series of ADS simulations were conducted to validate the PCB design before it was created. The model was created to simulate when an IR signal is incident upon the MEMS, since analyzing the response will validate the functionality of the PCB before designing and fabrication. A lumped distributed model of the MEMS was created by Matthew Benson, a PhD graduate student in our lab, and the S-parameter and Y-parameter responses were compared with the MEMS device that we have in the lab.

Each fabricated MEMS device is a piezoelectric resonator, and can be modeled with lumped components as a Modified Butterworth-Van Dyke circuit (mBVD) [7], as depicted in Figure 2.1(a). Rm represents the resonator loss, Lm is the mass of the resonator, Cm is the stiffness of the resonator, Co is the electrical capacitance between the MEMS and aluminum nitride layer, Ro is the dielectric loss associated with the electrical capacitance Co, Cp models the shift when an infrared light is incident onto the device.

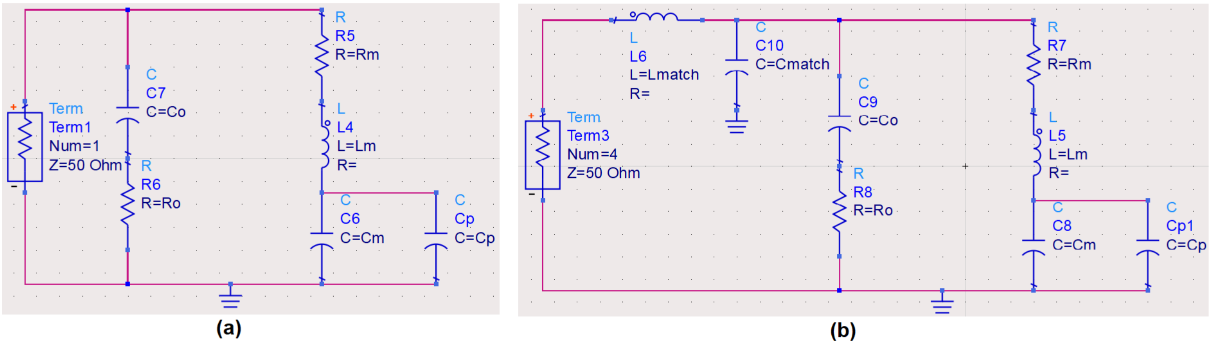

Figure 2.1: MEMS mBVD model in ADS (a) Without MN (b) With MN.

For initial testing of the model, Cp is set equal to 0, since it exists to model the shift response from an IR signal incident onto the MEMS. The actual MEMS resonator S-parameters and Y-parameters were measured using a vector network analyzer (VNA). Since the devices on the MEMS is a one port device, only the input reflection S(1,1) and input admittance Y(1,1) magnitude and phase responses were measured and compared. The comparison between the actual MEMS device and the ADS model without matching network (MN) is shown in Figure 2.2.

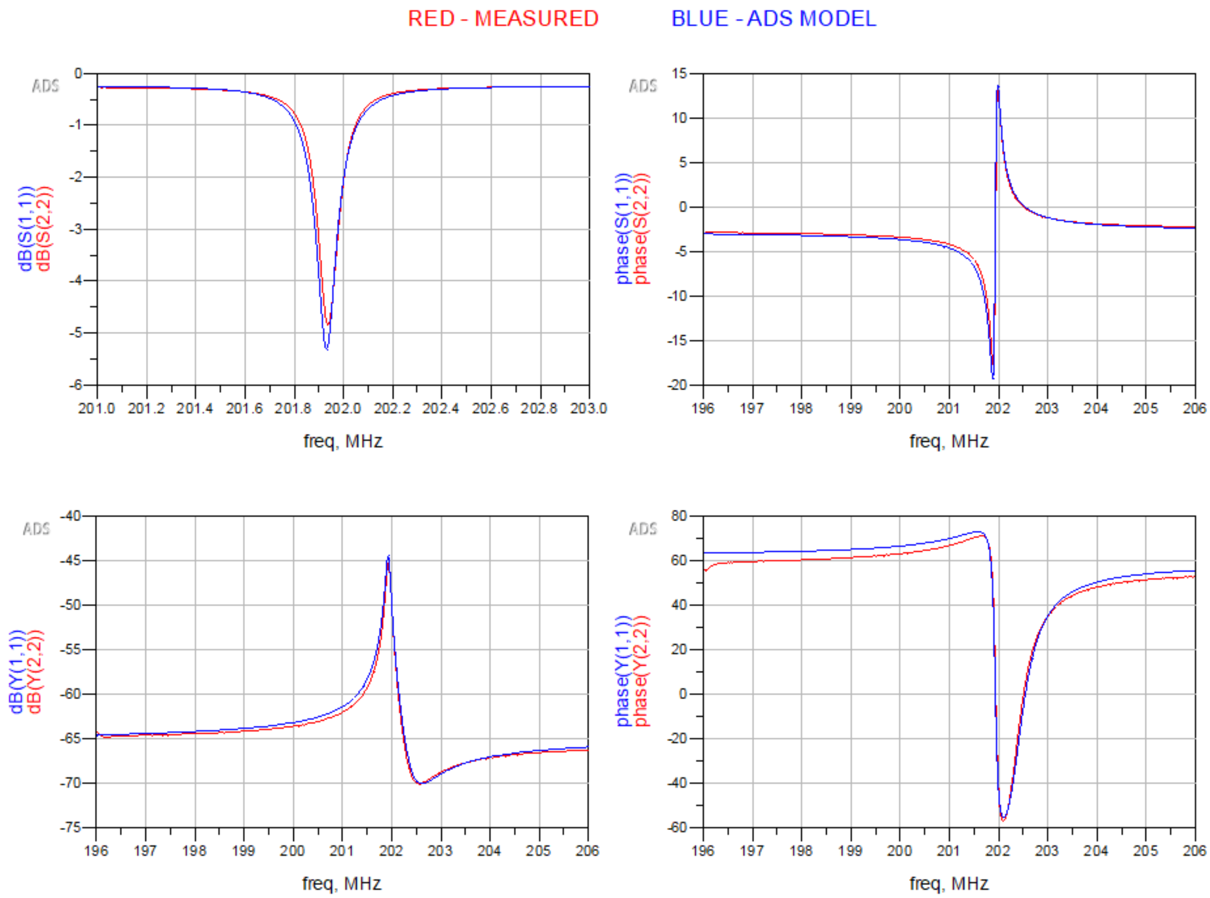

Figure 2.2: S-parameter and Y-parameter magnitude and phase response of actual MEMS device vs. ADS mBVD model (Without MN).

S(1,1) and Y(1,1) (red) correlate to the actual fabricated MEMS device , while S(2,2) and Y(2,2) (blue) correlate to the MEMS ADS mBVD model. It can be seen that the response of the ADS model is nearly identical to the measured response from the actual device, implying that the model is valid for continued simulations. For subsequent simulations, only the input reflection magnitude and phase will be analyzed and compared.

A variation of the model includes a low pass LC matching network, as depicted in Figure 2.1(b). The LC matching network was designed using ADS' smith chart tool to match a 50 Ω source with the load of our MEMS device. The idea behind using a matching network is to increase the responsivity of the MEMS device by increasing the selectivity, which directly correlates to the quality factor of the system:

$$Q = \frac{f_o}{\Delta f} \qquad \text{where } \Delta f \text{ is the bandwidth} \tag{2.1}$$

The tradeoff of a higher quality factor is that the bandwidth of the system decreases, so the resonance is narrower and more sharply defined, as observed in the magnitude response of Figure 2.3. Therefore, the circuit will respond stronger to the signal near or at resonance compared to a system without a matching network. This desired effect results in the selectivity increasing, which means that the responsivity of the MEMS device also increases.

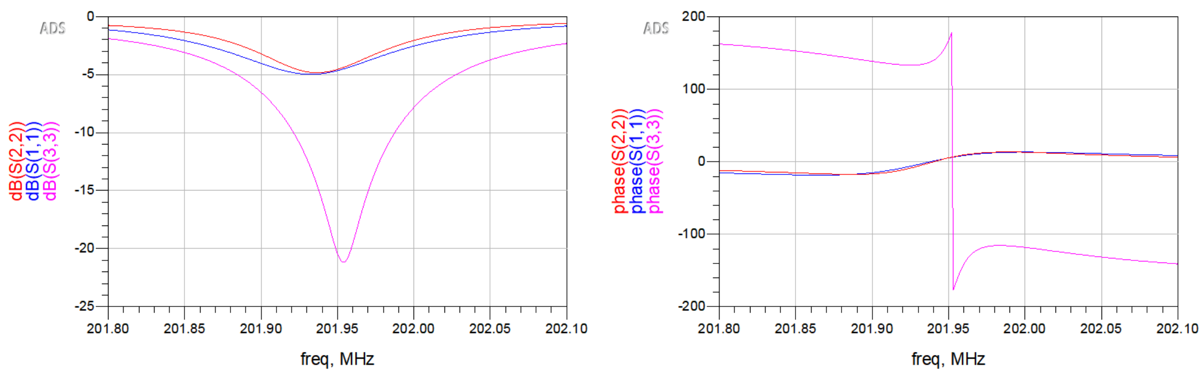

Figure 2.3: Magnitude and phase response of actual MEMS device (S(1,1)) vs. ADS mBVD model without MN (S(2,2)) vs. ADS mBVD model with MN (S(3,3)).

To more accurately represent the set-up in the lab, a coaxial cable was added into the simulation circuit. The coaxial cable adds additional parasitic capacitance and inductance that affect the resonance response. Therefore, this requires that the capacitance and inductance values of the matching network to be adjusted. The schematic, along with the magnitude and phase response of the mBVD model in ADS with the coaxial cable utilized in the lab, is depicted in Figure 2.4 and Figure 2.5 below. S(3,3) correlates to the mBVD model without an MN and S(4,4) correlates to the mBVD model with an MN.

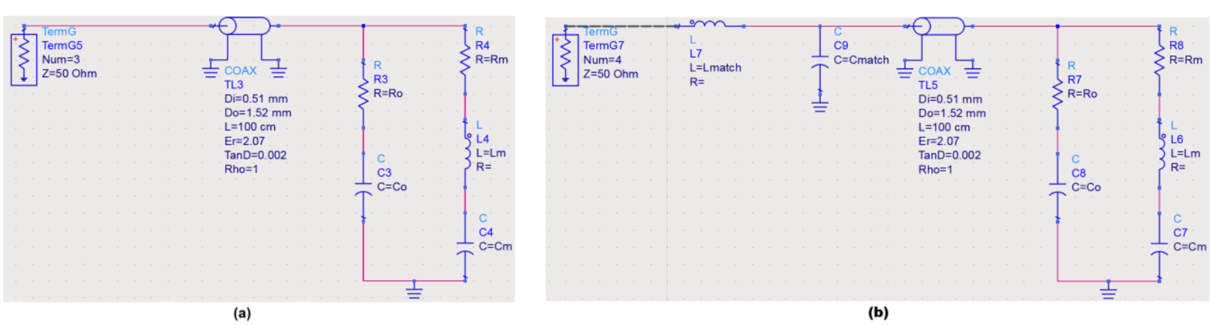

Figure 2.4: ADS MEMS mBVD model with addition of coaxial cable (a) Without MN (b) With MN.

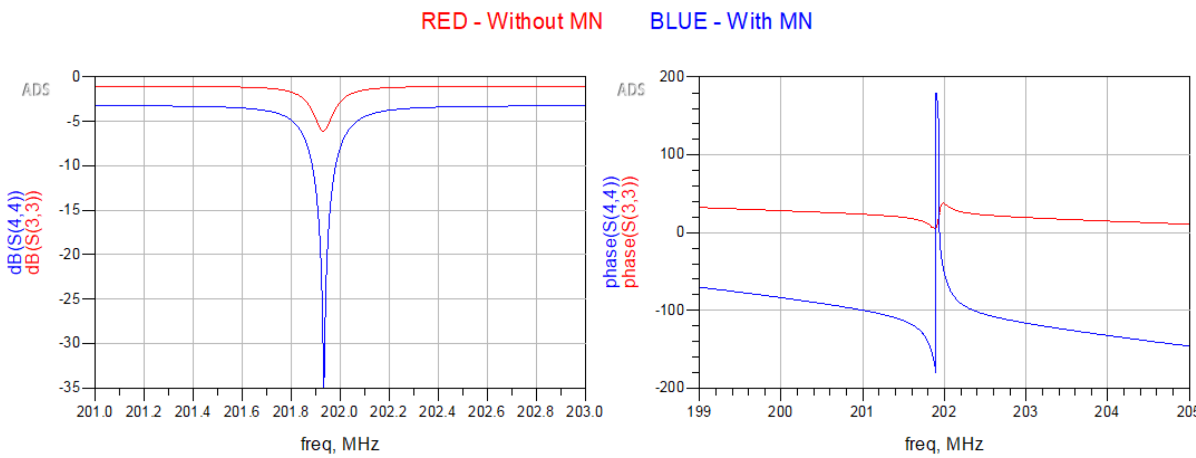

Figure 2.5: S-parameter magnitude and phase response of ADS MEMS mBVD model with coaxial cable without MN (red) vs. with MN (blue).

2.2 Choosing SMD Components for PCB

This section will discuss the surface mount devices (SMD) for the PCB that were chosen. Referring back to the RF section of Figure 1.5, the components of importance are the power splitter, directional coupler, LNA, and RF comparator. The bench-top set-up consists of only external components, so those components were used as a reference for choosing the SMD equivalents. The goal is to choose SMD components that offer similar or better performance than the bench-top counterpart. The chosen SMD components were then imported into ADS and simulated to ensure the functionality of the system. Table 2.1 displays the external components used for the bench-top set-up and the chosen equivalent SMD components. The operating frequency is around 200 MHz, so the component specifications discussed are analyzed at or around that frequency.

Component	Bench-top	SMD
Power Splitter	Z99SC-62-S+	ADP-2-4+
Directional Coupler	ZFDC-20-4+	ADC-20-132+
LNA	ZFL-500LN-BNC+	TQP3M9035
RF Comparator	4002 Phase-Gain Detector Module	AD8302

Table 2.1: Summary of bench-top external components and SMD components

The chosen SMD equivalent for the power splitter is Minicircuit's ADP-2-4+. The important parameters for the power splitter are the operating frequency range, isolation between the two splitter ports, amplitude and phase unbalance, and VSWR. The ADP-2-4+ offers a wideband operating frequency range from 0.5 MHz to 600 MHz and has a higher isolation, typically 24 dB compared to the bench-top counterpart where the isolation is typically 20 dB. Amplitude and phase unbalance defines the variation between the split signals. The amplitude and phase unbalance for the chosen SMD power splitter is typically 0 dB and 0.2 degrees, which is identical to the bench-top counterpart. The VSWR of the input port for both components were identical, around 1.2, whereas the VSWR of the split ports was higher at typically 1.25 compared to typically 1.1 with the bench-top counterpart.

The chosen SMD equivalent for the directional coupler is Minicircuit's ADC-20-132+. The important parameters are the operating frequency range, directivity, and mainline loss. The ADC-20-132+ operates from 100 MHz to 1300 MHz. Directivity is a measure of how well opposite traveling signals in the coupled port are isolated from each other. The ADC-20-132+ has a typical directivity of 24 dB, whereas the bench-top directional coupler has a typical directivity of 27 dB. Mainline loss is defined as the loss between the input and output ports. Both SMD and bench-top components have a mainline loss of around 0.4 dB.

The chosen SMD equivalent for the LNA is Qorvo's TQP3M9035. The important parameters for the LNA are the operating frequency, noise figure, gain, output third order intercept point (OIP3), and compression point (P1dB). The operating frequency range of the TQP3M9035 is from 50 to 6000 MHz and provides a gain of around 27 dB, compared to the bench-top amplifier, where the gain is 28 dB. However, the bench-top LNA is biased with a higher voltage compared to the TQP3M9035. Noise figure is a measure of how much noise the amplifier contributes, and the TQP3M9035 offers a very low noise figure around 0.55 dB versus the bench-top LNA with a noise figure of around 3.03 dB. For the purposes of this project, IP3 and P1dB are figures of merit for linearity of the amplifier. The TQP3M9035 has an OIP3 of 37 dBm and P1dB of 22.5 dBm, whereas the bench-top LNA has an OIP3 of 14 dBm and P1dB of 7.7 dBm.

In the bench-top set-up, the Valon 4002 was utilized as external component that housed and shielded the RF comparator integrated circuit (IC) and provided SMA connectors for the input and output ports. The actual RF comparator IC is the AD8302 from Analog Devices, which will be utilized in the PCB.

2.3 PCB Simulations

After choosing the SMD equivalent components for the bench-top set-up, the goal is to replicate an IR power sweep experiment in ADS with the SMD components to ensure that the system functions properly with the chosen SMD components. The IR power sweep experiment measures the magnitude and phase change between the reference signal and MEMS reflected signal across a range of IR powers incident upon the MEMS with different loaded Q matching networks. The S-parameters of the components were downloaded from the manufacturer's website and imported into ADS to create a model for the component. An example of the imported S-parameters for the LNA, TQP3M9035, and defined model from the S-parameters is shown in Figure 2.6.

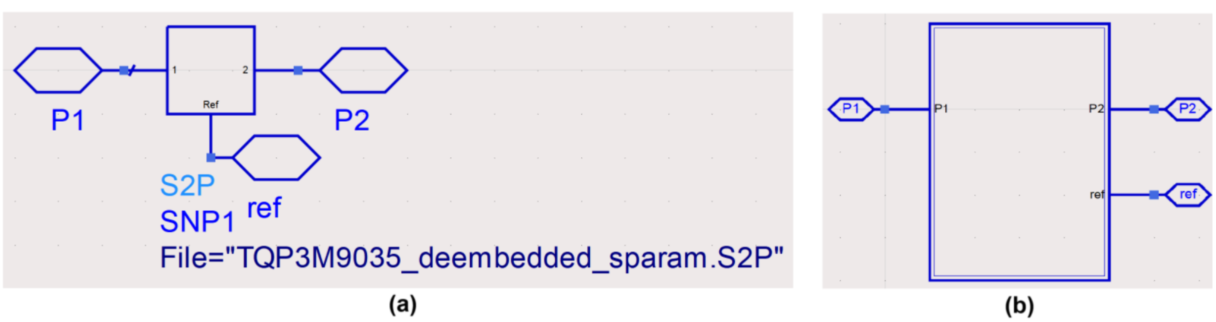

Figure 2.6: (a) LNA schematic with imported S-parameter (b) Model created from schematic.

Figure 2.7 and Figure 2.8 displays the ADS schematic of the replicated bench-top set-up. All the components except the RF comparator were imported and modeled in ADS. Only the input reflection (S(1,1)) of the RF comparator was provided by the manufacturer, therefore, not only is it modeled as a one port system, which would be invalid in this scenario, but it would also not be able to produce the output DC voltage response for magnitude and phase differences. However, by terminating the reference and reflected signal paths with a 50Ω load, the power at each termination can be measured. This allows the power difference between the reference and reflected signal from the MEMS to be computed, allowing us to convert that power difference into the RF comparator DC voltage response using a MATLAB script.

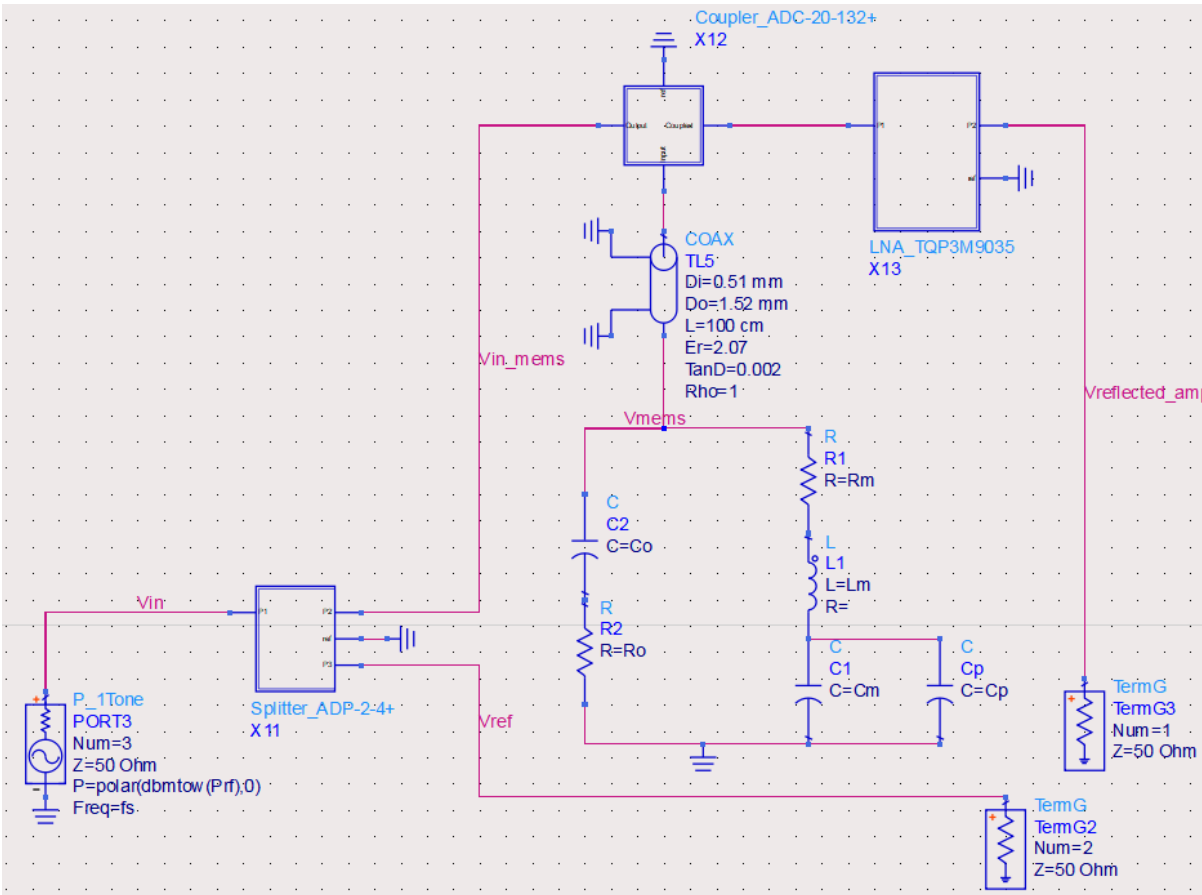

Figure 2.7: ADS bench-top set-up with SMD components (no MN).

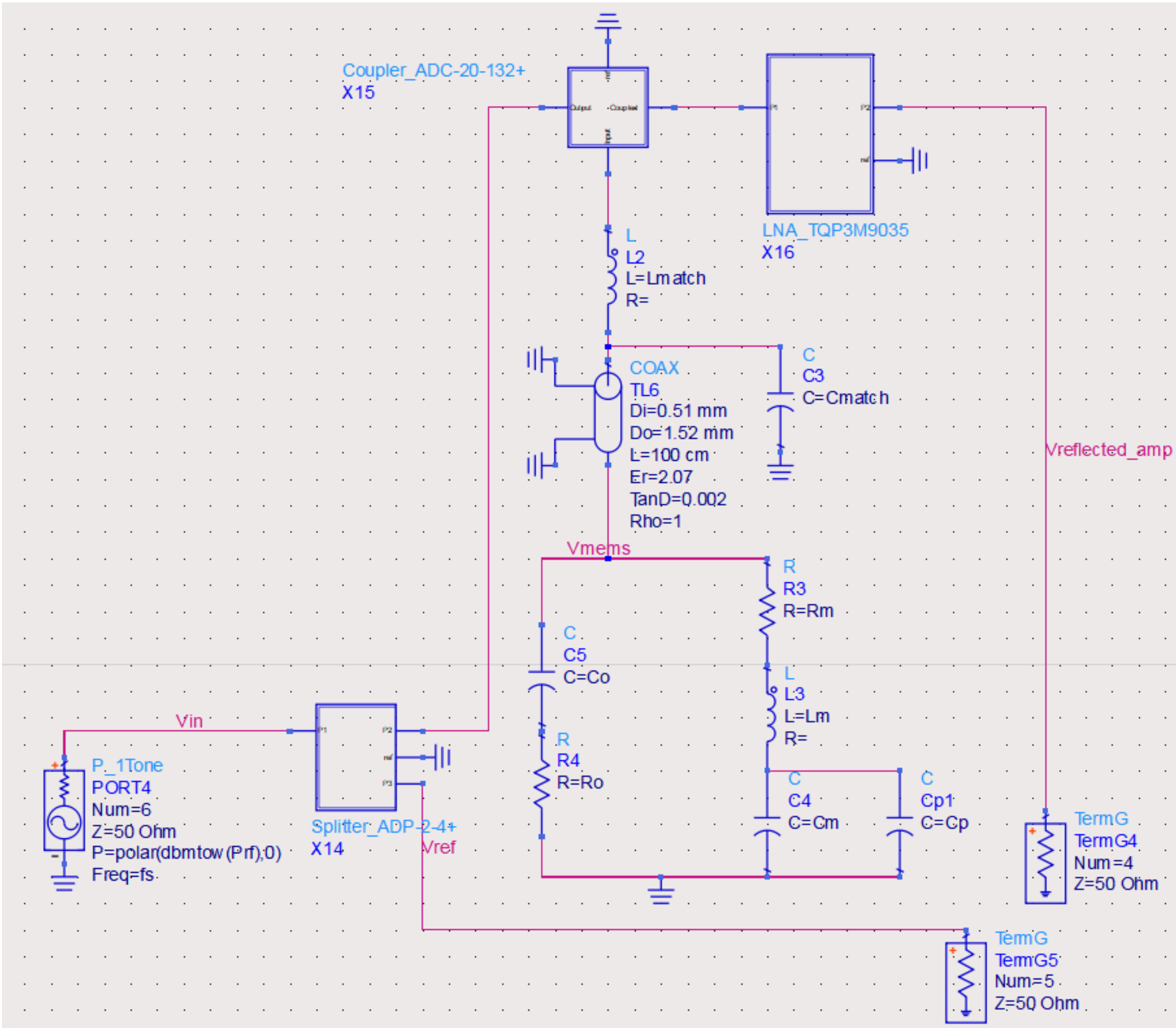

Figure 2.8: ADS bench-top set-up with SMD components (MN).

The MATLAB script was created by Matthew Benson, a graduate PhD student in our lab. The magnitude and phase power at the reference and reflected ports are imported into MATLAB. The data is formatted as [M × 2] matrix, where in the first column, M is the number of points taken during the IR power sweep, and the second column is the power at the reflected or reference port in dBm at the measured IR signal. First, the difference between the reflected and reference signal when there is no incident IR onto the MEMS is considered for calibration. Second, the difference between the reflected signal and reference signal is taken across the entire IR power sweep. To acquire the final output voltage value from the comparator that would be observed in an oscilloscope, the absolute difference is taken between the values acquired from the first step and second step, and multiplied by the magnitude response of the RF comparator (29mV/dB). An example code to acquire the magnitude DC output voltage is provided below:

```
% Values of RF detector responsivity
det_resp_mag = 29;  % 29 mV/dB from datasheet @ ~100 MHz, 30 @ ~900 MHz

% Consider signal with no IR.
ref_mag = (Pref_mag(1,2)-Pmems_mag(1,2));

% Consider signal with IR.
IR_mag = (Pref_mag(2:end,2)-Pmems_mag(2:end,2));

% Signal on lock-in (peak to peak)
sig_mag_V = abs(IR_mag-ref_mag) * det_resp_mag;
```

For simplicity, since the phase response provides higher responsivity, only the phase change is analyzed when the system has a matching network with a loaded Q of 19k and when there is no matching network, which has a loaded Q of 1.6k. The comparison between the bench-top experimental results and the simulated SMD set-up results are plotted in MATLAB. Figure 2.9(a) displays the phase change response across the IR power sweep at different loaded quality factors with the bench-top set-up in the lab that has external components. Those results are analyzed and overlapped with the SMD set-up in Figure 2.9(b-c) for when there is no matching network and for when a matching network with a high quality factor is utilized. The plots convey that the SMD set-up matches well with the results from the bench-top set-up, therefore, it verifies the functionality of the system and that these SMD components are appropriate equivalents for the external components in the bench-top set up.

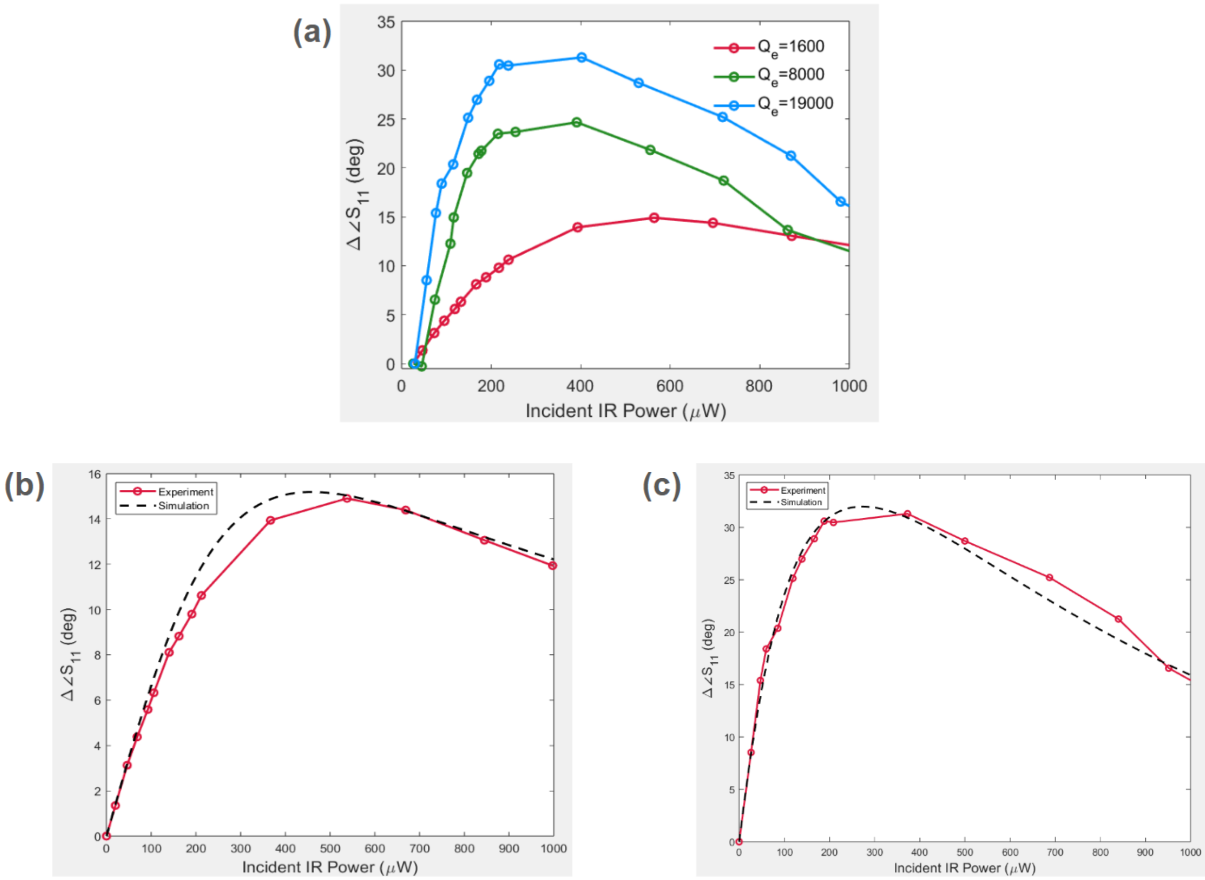

Figure 2.9: IR power sweep bench-top set-up experimental results vs. ADS SMD set-up results (a) Bench-top IR Power Sweep Results (b) Qe = 1.6k bench-top set-up vs SMD set-up simulation (c) Qe = 19k bench-top set-up vs SMD set-up.

Apart from replicating the entire IR power sweep experiment to test the functionality of the PCB, a test point is added to ensure that the correct signal is observed when reflected from the MEMS and through the coupled port of the coupler. The outputs of the LNA and the other splitting port of the power splitter are terminated with 50 Ω to replicate that all the signal should ideally be transmitted to the RF comparator. The simulation for this test point schematic is shown in Figure 2.10. The second termination is where an SMA connector will be added to the PCB to use as a test point. By adding a termination at the RF input and a termination after the coupled port of the directional coupler, we can observe the input reflection S(1,1) and forward transmission S(2,1).

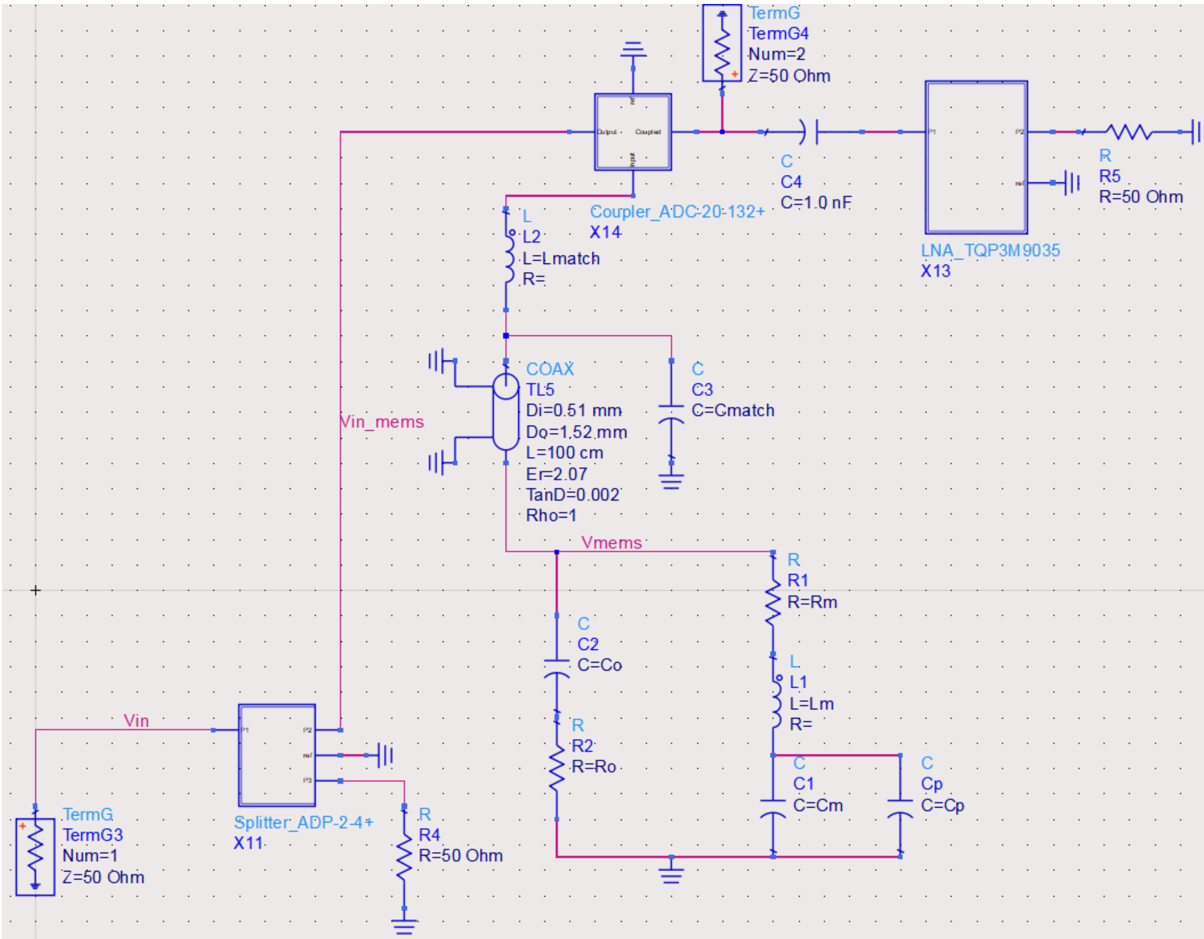

Figure 2.10: Test point with MN ADS schematic.

S(1,1) measures the reflected signal from the MEMS that travels back through the directional coupler and power splitter. Since the mainline loss of the coupler is around 0.4 dB and there is no isolation between the input and output ports, the reflected signal from the MEMS can be observed by measuring S(1,1) using a VNA. S(2,1) measures the reflected signal from the MEMS that is transmitted to the coupled port of the coupler. The expected result is that the S(2,1) should have the same response as the S(1,1), but at a lower power because the transmitted signal travels through the power splitter and coupled port of the coupler, which results in a loss of around 23 dB. The phase response will also have an offset between the S(1,1) and S(2,1) because of the difference in path length. The expected result without an MN is displayed in Figure 2.11, while Figure 2.12 displays the expected results with an MN.

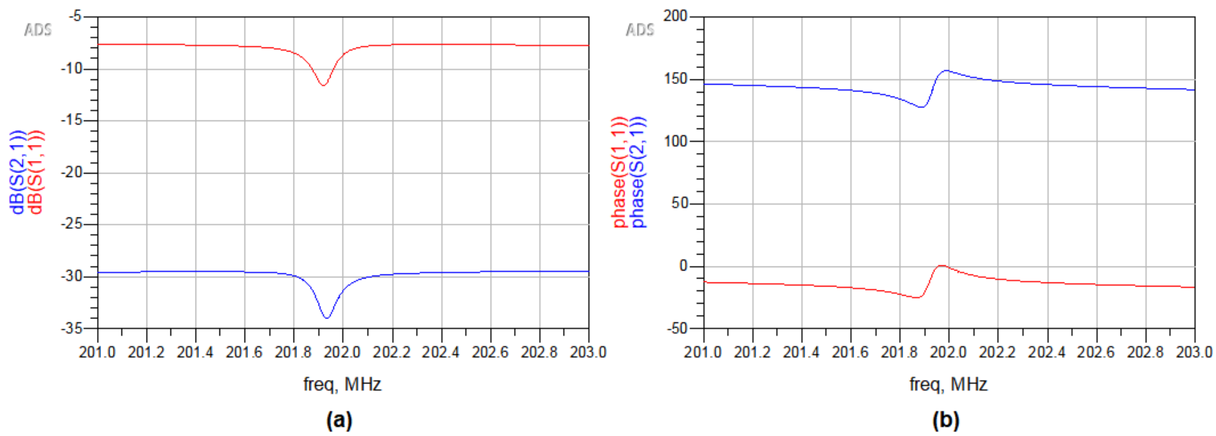

Figure 2.11: Test point without MN S-parameter Results (a) Magnitude response (b) Phase response.

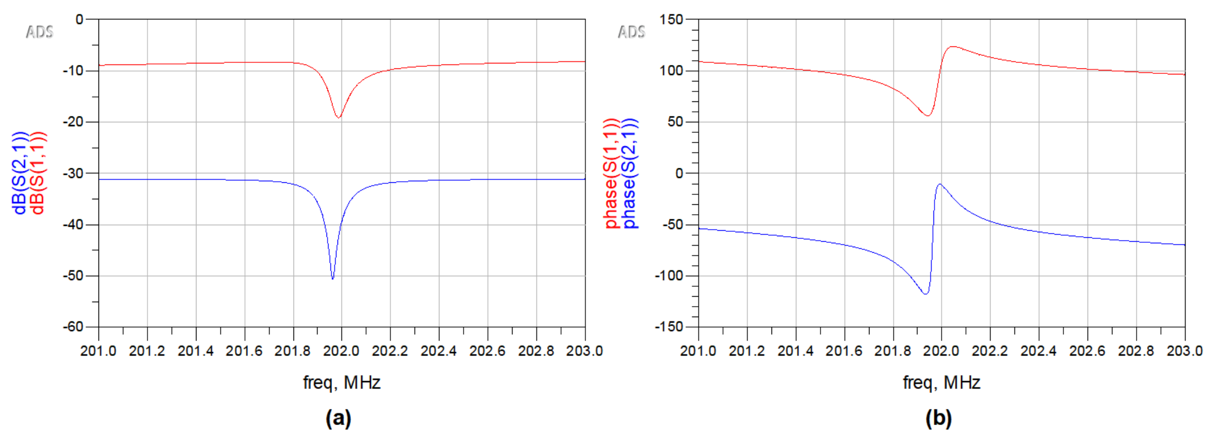

Figure 2.12: Test point with MN S-parameter Results (a) Magnitude response (b) Phase response.

Chapter 3

PCB Design & Testing

3.1 Trace Impedance

To maintain signal integrity and minimal reflection, it is important to match the impedance of the traces of the PCB to the rest of the components and connectors (50 Ω). The stack-up for a typical 2-layer PCB consists of the top solder mask, top copper layer, dielectric core, bottom copper layer, and bottom solder mask. The copper traces atop of the dielectric substrate are microstrip planar transmission lines, and its characteristic impedance is dependent on the operating frequency and geometry of the microstrip. The derivation and discussion of the impedance of a microstrip line is referenced to M.V Schneider's "Microstrip Lines for Microwave Integrated Circuits" [8]. The impedance of is calculated using the characteristic impedance and effective dielectric constant of the microstrip:

$$Z = \frac{Z_o}{\sqrt{\epsilon_{eff}}} \tag{3.1}$$

Using Schwarz-Christoffel transformation and rational function approximation, the approximated solution for the characteristic impedance can be found assuming that the thickness of the trace is 0, therefore, negligible. The analytical characteristic impedance formula is expressed as a relation of w and h, the width of the microstrip and the height of the dielectric substrate to the reference plane, respectively:

$$Z_o = 60 \ln \left(\frac{8h}{w} + \frac{w}{4h} \right) \qquad \text{for } \frac{w}{h} \leq 1 \tag{3.2}$$

$$Z_o = \frac{120\pi}{\frac{w}{h} + 2.42 - 0.44\frac{h}{w} + (1 - \frac{h}{w})} \qquad \text{for } \frac{w}{h} \geq 1 \tag{3.3}$$

The effective dielectric constant can also be derived from the same conformal mapping transformation and using irrational function approximation:

$$\epsilon_{ff} = \frac{\epsilon_r + 1}{2} + \frac{\epsilon_r - 1}{2}\left(1 + \frac{10h}{w}\right)^{-\frac{1}{2}} \tag{3.4}$$

This specific set of equations for the characteristic impedance and effective dielectric constant constitute just one of many representations for these parameters. Different representations for these parameters have been developed by numerous engineers. The more well known representations are presented in the various works by Wheeler, which were later modified by Hammerstad and Jensen [9, 10, 11, 12]. The different representations offer different levels of precision and complexity, but generally results in extreme accuracy.

For the purpose of this project, the impedance calculator by the PCB manufacturer, JLCPCB, was utilized to calculate the trace width required for 50 Ω traces. The initial idea was to utilize a 1.6 mm (63 mil) thick, 2-layer board with the stack-up previously described. However, this results in a required width of around 106 mils for 50 Ω traces, while all the pins on the IC components were on the scale of 15-30 mils, as depicted with the example of the RF comparator pins below in Figure 3.1.

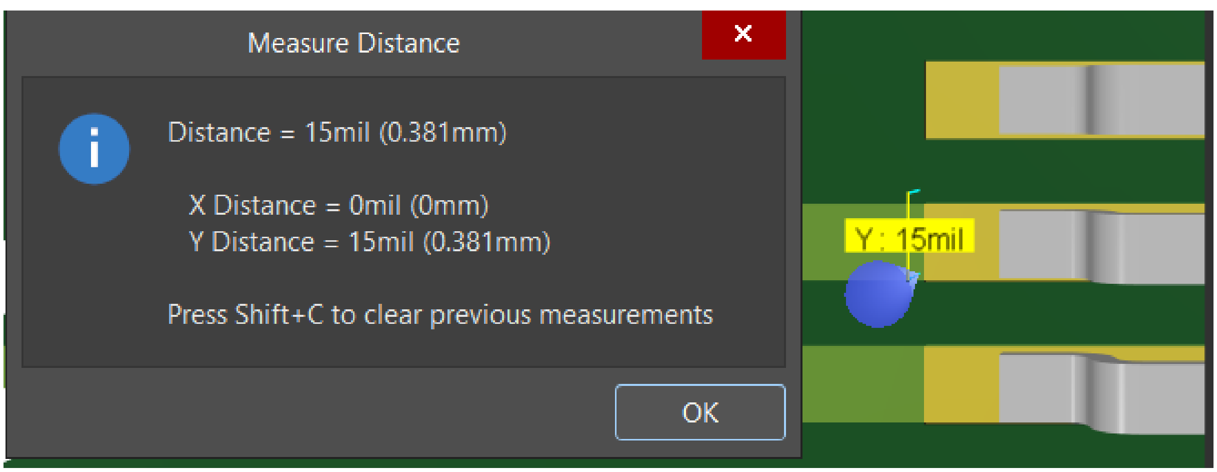

Figure 3.1: Width of RF comparator pin.

The significant transition from a thick trace to a smaller trace would cause reflection and distort the signal, so a potential solution would be to be taper the trace before connecting it to the IC pins. Tapering gradually widens or narrows the trace, so that the impedance change is not sudden. However, this would increase the complexity and space required for the PCB. From the previous expressed equations for characteristic impedance and effective dielectric constant, it is possible to reduce the width required for an impedance of 50 Ω by reducing the height of the dielectric layer between the signal layer and reference layer. Therefore, the proposed solution is to utilize a 1.6 mm (63 mil) thick, 4-layer board with the stack-up shown in Figure 3.2. This results in the thickness of the traces required for 50 Ω to be around 13.75 mils. Moreover, since the current traveling through the traces will be much less than 1A, we do not need to be concerned about the current handling capabilities of the trace.

Layer	Material	Thickness (mil)	Thickness (mm)
L1	Outer Copper Weight	1.38	0.0350
Core	1.5mm 1/1OZ with copper (double-sided)	57.68	1.4650
L2	Outer Copper Weight	1.38	0.0350

(a)

Layer	Material	Thickness (mil)	Thickness (mm)
L1	Outer Copper Weight1oz	1.38	0.0350
Prepreg	7628, RC 49%, 8.6 mil	8.28	0.2104
L2	Inner Copper Weight	0.60	0.0152
Core	1.1mm H/HOZ with copper	41.93	1.0650
L3	Inner Copper Weight	0.60	0.0152
Prepreg	7628, RC 49%, 8.6 mil	8.28	0.2104
L4	Outer Copper Weight1oz	1.38	0.0350

(b)

Figure 3.2: JLCPCB stack-up dimensions (a) 2-layer stack-up (b) 4-layer stack-up [13].

3.2 Design 1: Replicating Bench-top Set-up

The main goal of the first design is to replicate the bench-top set-up and test that the designed PCB matches with the ADS simulation results and the results from the bench-top experiments. Altium is utilized to design the PCB, and the discussed SMD components from the previous chapter are used in the design. The datasheet of the components provide the pin connections, and some provide recommended connections for an evaluation board, which will be followed for this design.

The connections for the power splitter are shown in Figure 3.3. The RF signal that excites the MEMS and used as reference is inputted into the summed port of the power splitter using a SMA connector. Pins 2 and 5 are connected to each other and isolated from the rest of the circuit. PORT1 of the splitter is connected to the RF comparator, while PORT2 is connected to the directional coupler for exciting the MEMS.

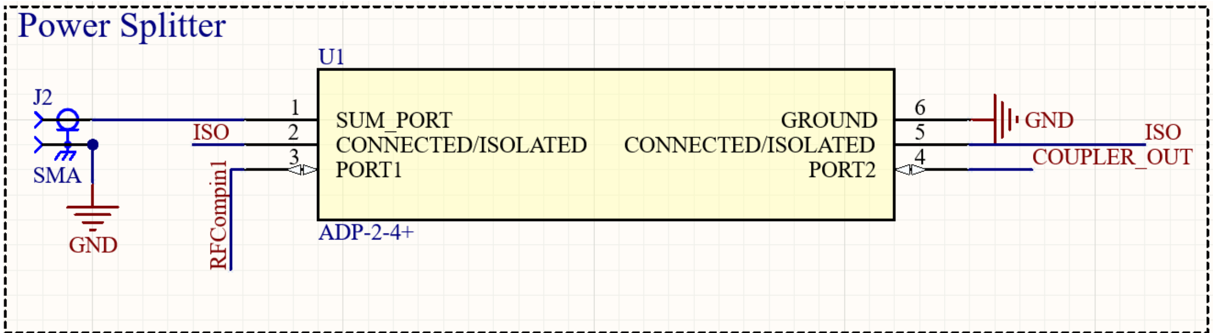

Figure 3.3: Power splitter schematic in Altium.

Figure 3.4 displays the schematic and equivalent model for the directional coupler. In reality, the directional coupler is a 4 port system, so one of the ports must be terminated with an external 50 Ω load to prevent reflections affecting the coupled port signal. The coupler also has an isolate port where it is specifically stated to not use. The excitatory RF signal is connected to the output of the coupler, since the reflected signal from the MEMS must be connected to the input port of the directional coupler for it to travel to the coupled port.

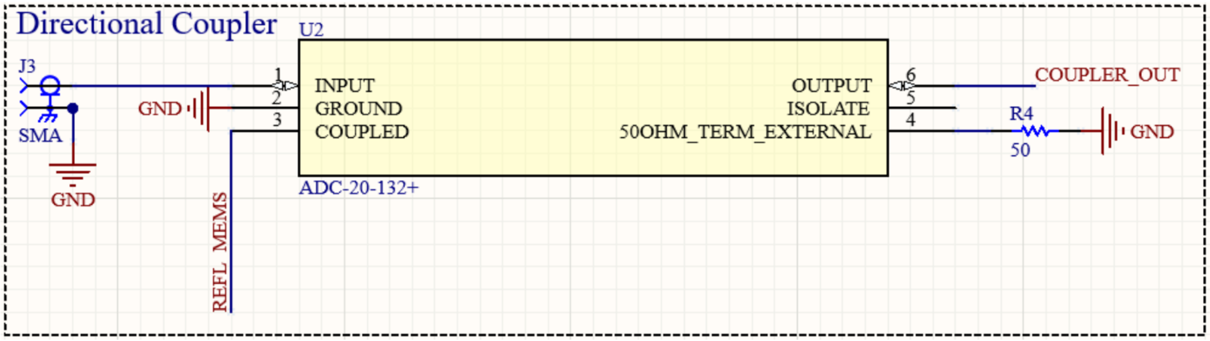

(a)

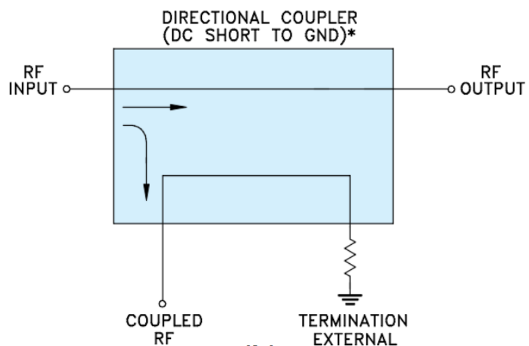

(b)

Figure 3.4: (a) Directional coupler schematic (b) Directional coupler equivalent model.

The 5V supply to bias the LNA and power the RF comparator is inputted using a connector, as displayed in Figure 3.5. C5 and C12 act as decoupling capacitors to suppress high frequency noise that might be from the power supply. The 0 Ω resistor, R1, is a snubbing resistor to lessen the stress experienced by the RF comparator from the transient voltage spikes during start up of the power supply.

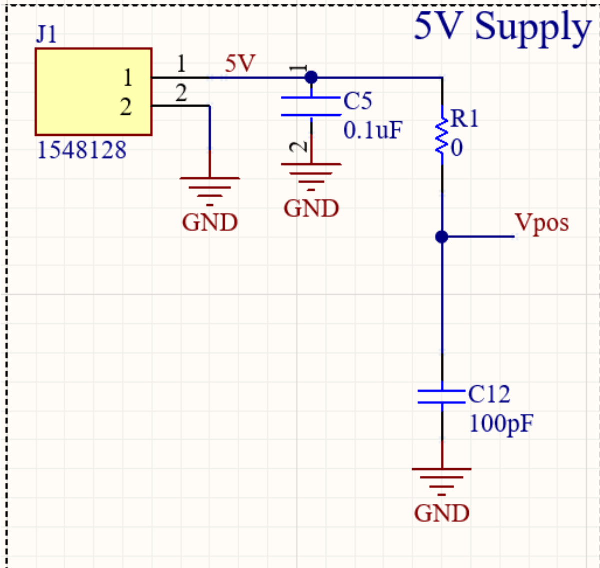

Figure 3.5: 5V power supply schematic in Altium.

The LNA schematic with a test point is depicted in Figure 3.6. The test point is a SMA connector represented by J1. The 1 nF capacitors C1 and C2 connected to the input and outputs of the LNA are intended to block DC signals to prevent interference with the RF signal. The value for the capacitor is chosen so that it exhibits low impedance at the operating frequency. At 200 MHz, the impedance of those capacitors is roughly 5 Ω. The LNA is biased with 5V via an RF choke inductor, L1, which passes the DC signal needed to bias the VNA, while blocking the higher frequency AC signals. C3 and C4 are decoupling capacitors for the power supply. The LNA offers a shutdown pin that shuts down the LNA if a certain threshold voltage is reached, but this feature is not utilized, so the shutdown pin is grounded. The N/A pins are for connectivity of the component onto the board.

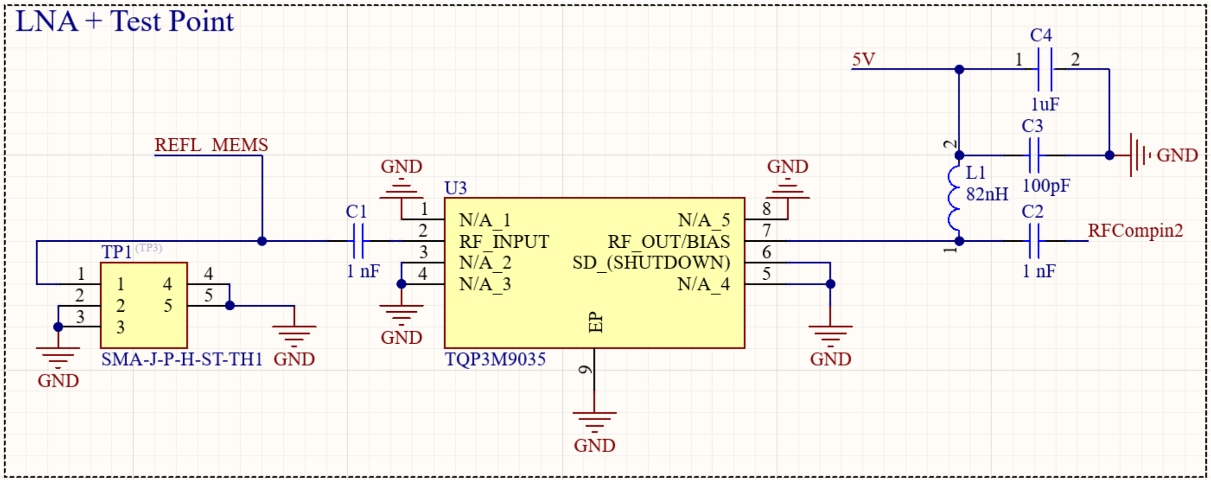

Figure 3.6: LNA & test point schematic in Altium.

Figure 3.7 displays the schematic for the RF comparator. The inputs INPA and INPB requires AC coupling capacitors and shunt 52.3 Ω termination. The COMM ports refer to a common ground and VPOS is the supply voltage. Since there is a total of 60 dB of cascaded gain, slight DC offsets can cause measurement errors for small signals. Therefore, there is an internal feedback loop that aims to cancel this offset. The high pass corner frequency of the feedback loop is set by OFSA and OFSB. It is recommended to use a capacitance of 1 nF for the compensation loop, which sets the high pass corner frequency to around 100 MHz. These capacitors also provide input decoupling by providing AC grounding. MFLT and PFLT is for low pass filtering both the magnitude and phase outputs, respectively. The value of the low pass capacitors depends on the noise observed at the output, so MFLT and PFLT is initially left open and C9 and C11 are placeholder capacitors. MSET and PSET are used to scale the magnitude and phase output voltage, and to acquire the desired response of the comparator presented in Figure 1.6(b-c), MSET must be shorted to VMAG and PSET must be shorted to VPHS. The outputs of the comparator are connected to SMA connectors to extract the signal to a lock in or oscilloscope. The VREF pin can be used as a testing point for the comparator to determine its functionality, since the reference voltage is constant at around 1.8V.

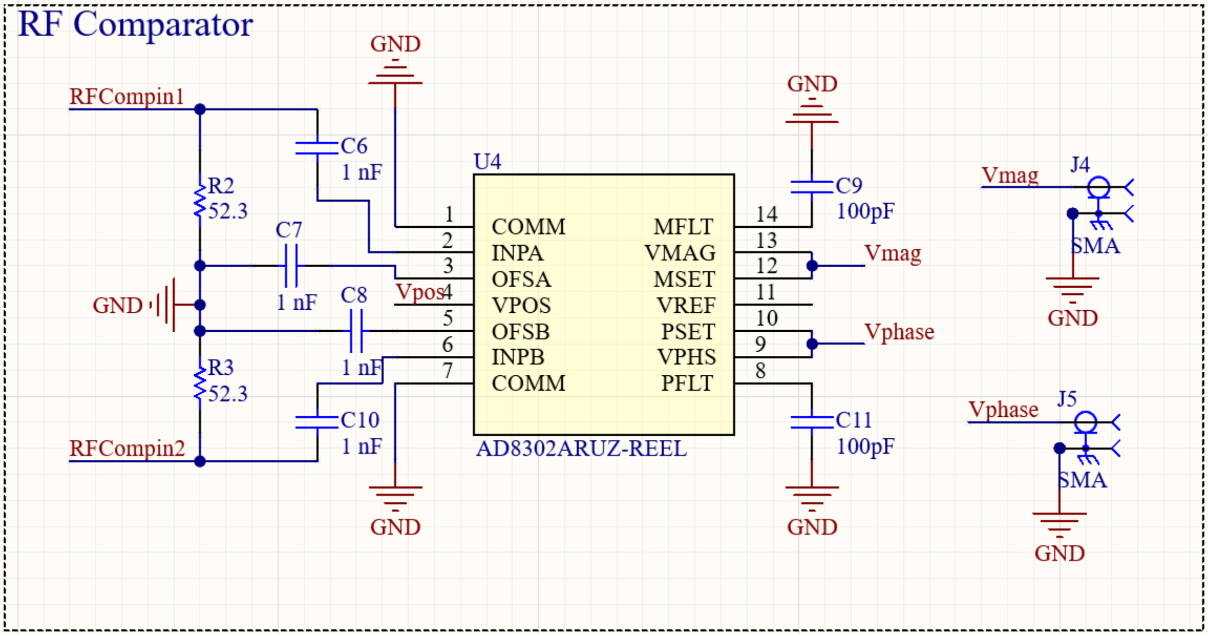

Figure 3.7: RF comparator schematic in Altium.

3.2.1 PCB Layout

After completing the schematic with that contains all the connections for the PCB and validating that the connects are correct, the design is ready for PCB layout. All the components contain a footprint, which is the physical area that the component takes up. The footprints of the components were imported from various supplier sites including Mouser and Digikey. The netlist that defines the circuit's electrical connections between component pins is automatically set up by Altium, so that the user can only make valid connections based on the schematic connections. The completed PCB layout is displayed in Figure 3.8.

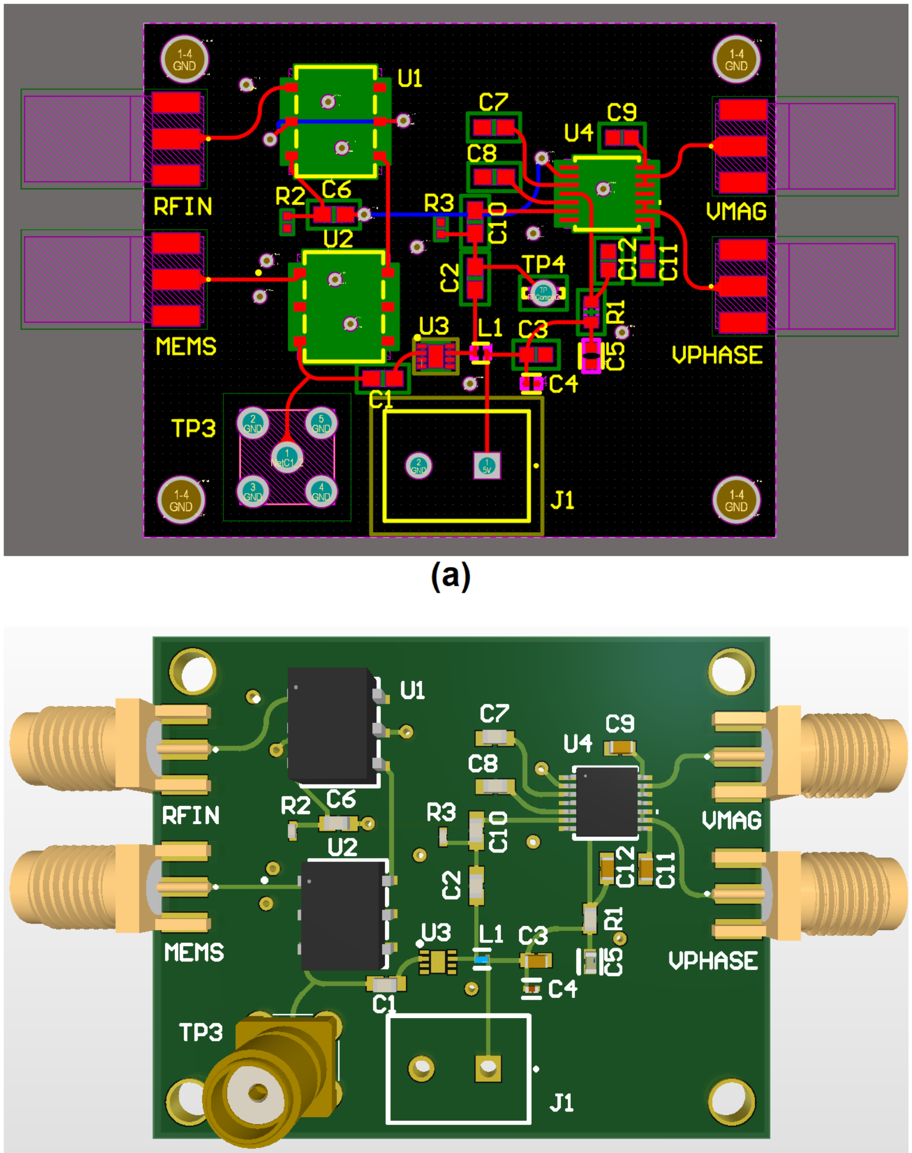

(a)

(b)

Figure 3.8: Design 1 PCB Layout (a) 2D model (b) 3D model.

The board is a 4-layer board, but only the top and bottom layers are used for electrical signal. The red traces represent the connections on the top layer, while the blue traces represent the connections on the bottom layer. The inner layers are used as ground planes. After completion of the PCB layout, the Gerber files are exported and sent for manufacturing.

3.2.2 Soldering Process

Since the SMD components are very small, it is not feasible to manually hand solder all the SMD components. Therefore, the Diane Bryant Engineering Student Design Center (ESDC) was utilized for the soldering process, as they have a reflow oven that makes the soldering process quick and easy. The soldering steps are displayed below in Figure 3.9

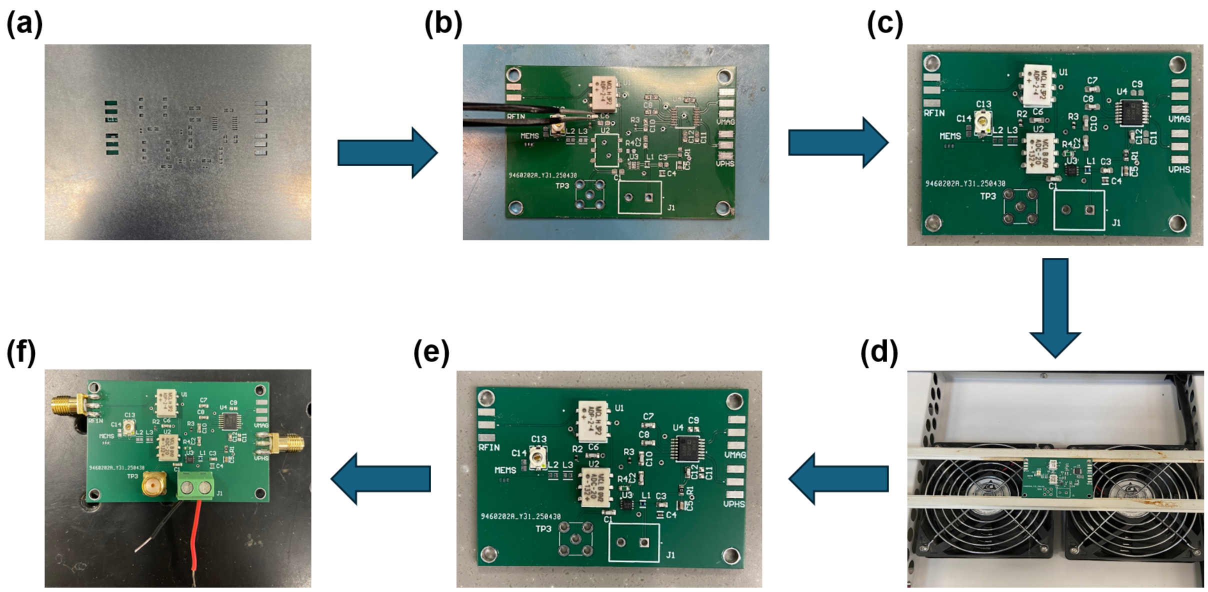

Figure 3.9: PCB soldering process (a) Place stencil on board and apply solder paste (b) Place components on pads (c) Inspect components (d) Place PCB into reflow oven with configured profile (e) Inspect soldered board (f) Solder through-hole components and SMA connectors.

Referring to the above, first, a stencil that has a cutout of all the SMD pads is layered and aligned onto the PCB. Using the stencil, solder paste is applied to the PCB pads and the components are placed onto the pads. The components are checked to make sure they are aligned onto the pads. Then, the board is placed into a reflow convection oven, where it undergoes a specific process that warms up the board and slowly heats up to the temperature required to melt the solder paste. The reflow oven profile is especially important in ensuring that the solder paste undergoes the process needed to solder the components onto the pad. The datasheet of the solder paste that is utilized displays a few example profiles for the reflow process in Figure 3.10. The paste has a melting point of 217°C.

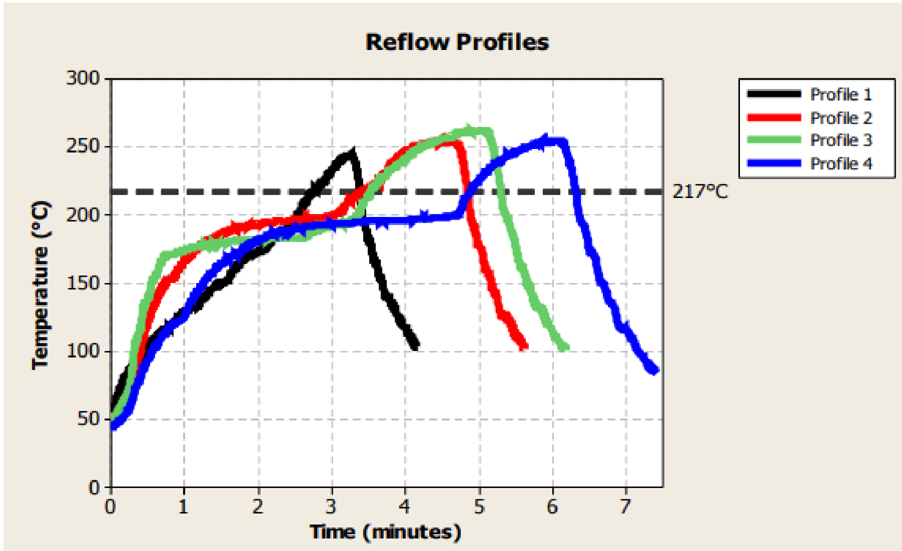

Figure 3.10: LOCTITE GC 10 example reflow profiles [14].

There is no specific reflow profile that works for all applications or pastes, so various reflow settings were tuned and tested. The soldering process with a reflow oven is analogous to baking. The board needs to be preheated to a certain temperature, then the temperature should slowly increase past the melting point of the paste until it reaches a peak temperature before cooling down and letting the paste set. The profile developed first warms up the reflow oven to 160°C, and once the board is placed into the oven, the board is preheated to 160° for 160 seconds. Note that the temperature displayed is measuring the temperature of the convection oven, so the board temperature may be lower. After warming up, the oven is heated up to 230° for 95 seconds. The temperature reaches 230° before the entire interval, so it hovers around that temperature until this step is finished. Then, the board goes through the reflow process where the oven temperature is set to 260° for 70 seconds. Lastly, the board is left to cool.

After completing the reflow process, all of the SMD components should be properly soldered on. Each component is manually inspected to ensure that the components are properly soldered. Lastly, the SMA connectors and through hole components are manually hand soldered. The completed board for the first design is displayed in Figure 3.11

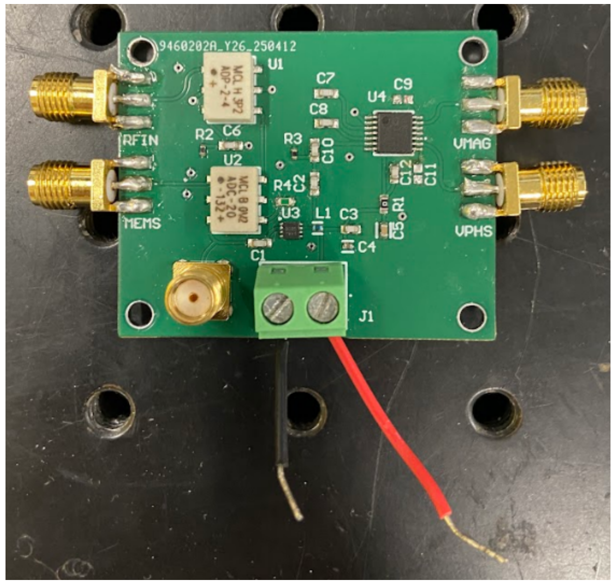

Figure 3.11: Design 1 soldered board.

3.2.3 Testing Functionality of Board

After soldering the board, the initial test is to power the board and confirm that it is drawing the correct range of current and power. The only active components are the LNA and RF comparator. During its on state, the LNA and RF comparator draws a total current of about 135mA, which was observed. For initial testing, a matching network was utilized. The next test is to ensure that the signal traveling through the coupled port of the coupler is identical or similar to the response observed from the ADS simulation. Using a VNA, the RF input SMA is defined as the first port and the test point is defined as the second port. The magnitude and phase response for the input reflection S(1,1) and forward transmission S(2,1) are measured and displayed in Figure 3.12 and Figure 3.13.

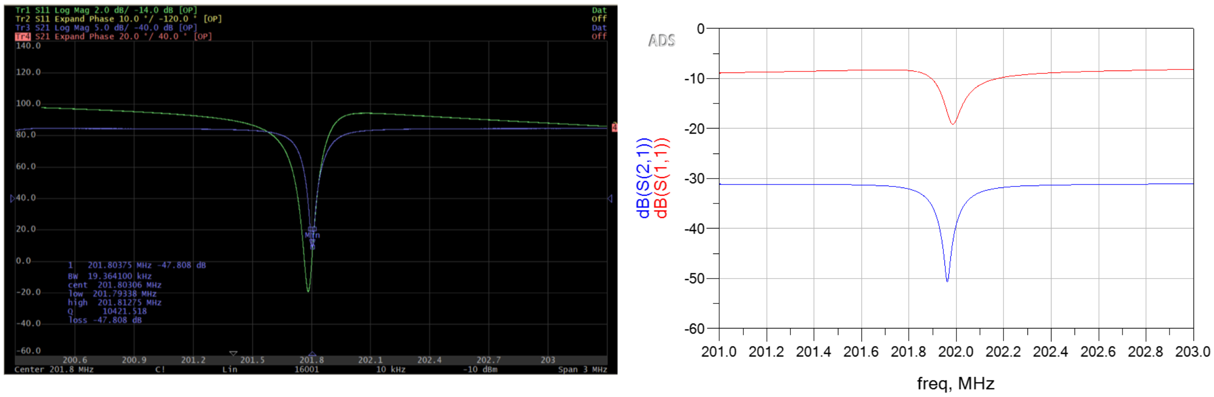

Figure 3.12: Test point VNA measurement versus ADS simulation S(1,1) and S(2,2) magnitude response

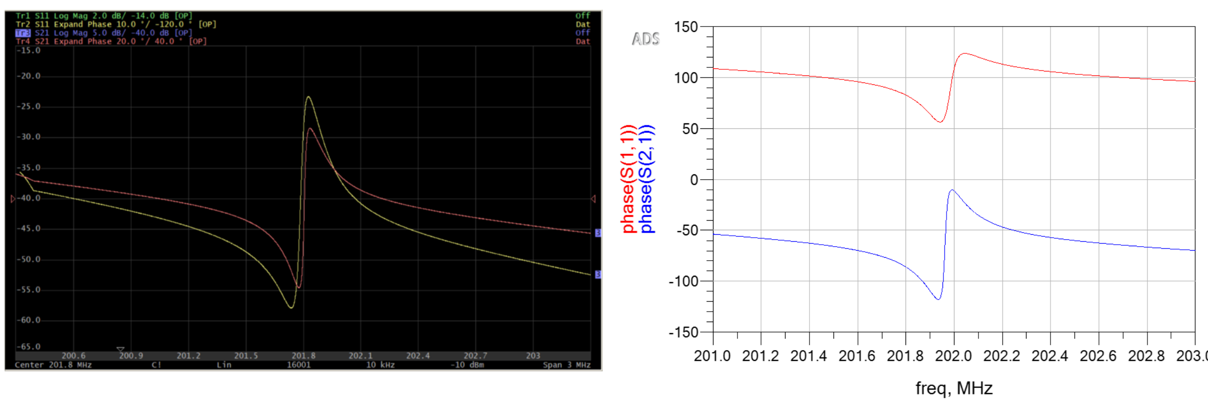

Figure 3.13: Test point VNA measurement versus ADS simulation S(1,1) and S(2,2) phase response.

The S(1,1) and S(2,1) VNA measurements are referenced at different scales, but it can be observed that their magnitude and phase response is similar to the response observed in the ADS simulation. The S(1,1) and S(2,1) will have the same response, but the S(2,1) will differ because of additional losses incurred by traveling through the coupled port of the coupler and the different path length causes a phase shift. Therefore, this preliminary test conveys that the correct signal is traveling to the RF comparator.

3.2.4 Replicating IR Power Sweep Experiment

To fully confirm the functionality of the designed PCB, the IR power sweep experiment that was conducted with the bench-top set-up is conducted with the PCB. However, since the bench-top IR power sweep experiment was done last year by the PhD students in our lab, the test conditions will have slightly changed. For this experiment, a different MEMS and wavelength is utilized, but the similar responses should be observed. The experiment observes the phase and magnitude response as the IR power incident upon the MEMS is swept and with matching networks of different loaded Q. The comparison between the magnitude response of the experiment with the bench-top set-up vs. PCB set-up bench-top below in Figure 3.14. Likewise, the phase response of the experiment is depicted in Figure 3.15.

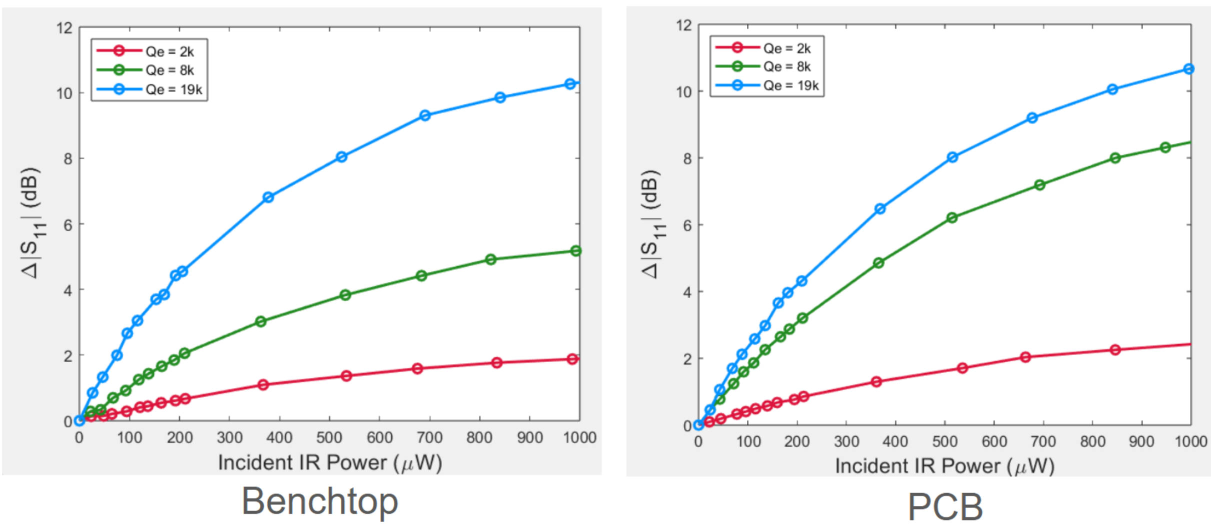

Figure 3.14: IR power sweep experiment bench-top vs. PCB set-up magnitude response.

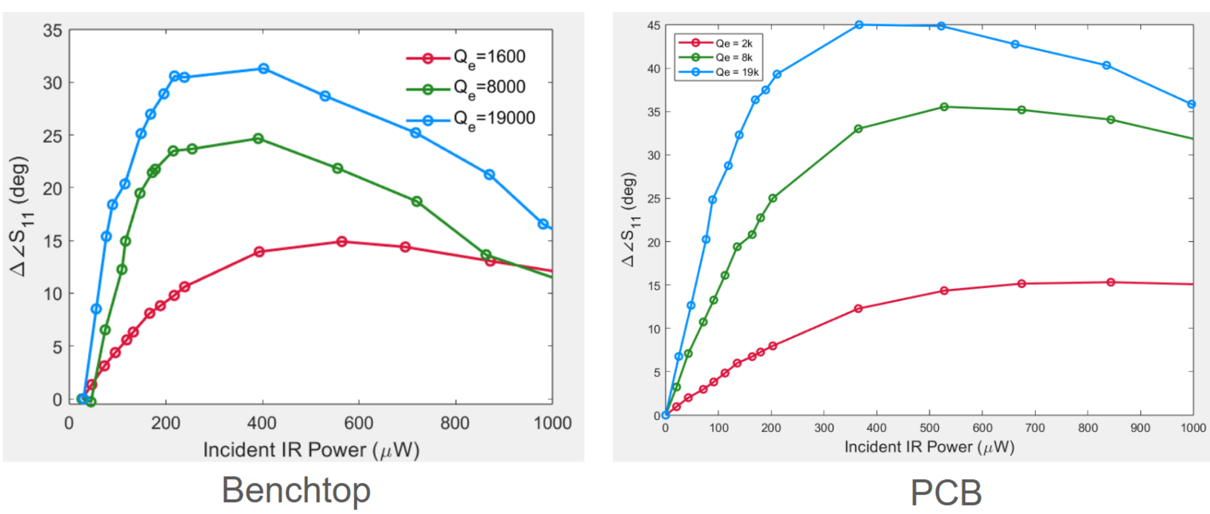

Figure 3.15: IR power sweep experiment bench-top vs. PCB set-up phase response.

As discussed, the results should not be the same, as a different MEMS device and wavelength was utilized for the experiment. However, the importance is the general behavior of the phase and magnitude change response as the incident IR power onto the MEMS changes. The expected and observed response is that the phase change and magnitude change is proportional to the incident IR power onto the MEMS up to a certain IR power, where the device's response saturates, and no longer exhibit a linear response. Replicating the experiment confirms the functionality of the PCB, as we are able to observe the expected magnitude and phase behavior versus IR power. The responsivity can also be determined by taking the slope of the magnitude or phase response. The maximum responsivity response is displayed in Table 3.1

Loaded Q	**Phase Max Responsivity (V/W)**	**Magnitude Max Responsivity (V/W)**
2k	475	131
8k	1431	582
19k	3700	935

Table 3.1: Max responsivity values for different loaded Q's

3.3 Design 2: Incorporating Arduino & Signal Generator

For the second design of the board, the goal is to use an Arduino Nano to process the magnitude and phase change data, while also having a standalone RF signal generator. This design is crucial in miniaturizing the system for the desired cancer-detecting device previously discussed. Figure 3.16 displays the schematic for the Arduino Nano.

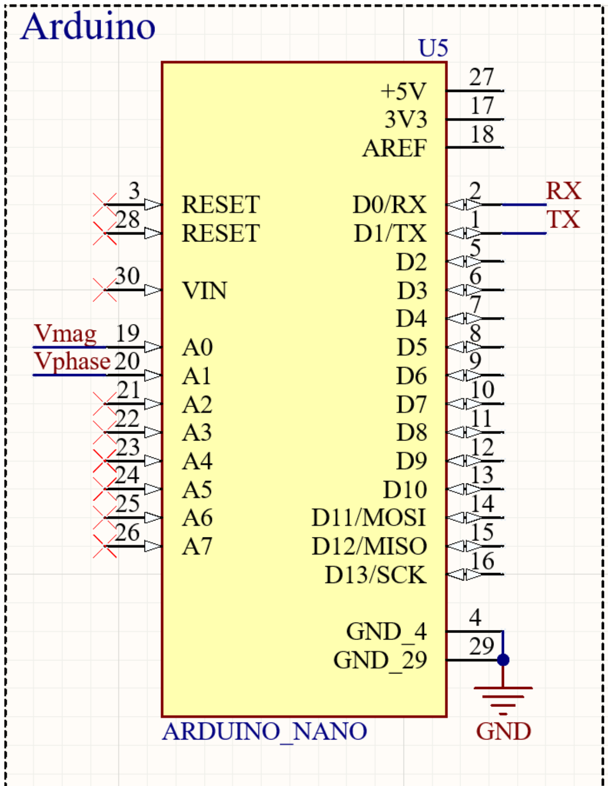

Figure 3.16: Arduino schematic in Altium.

In the previous design, the magnitude and phase voltage outputs from the RF comparator were connected to SMA connectors, so that the voltages could be read by a lock-in or oscilloscope. However, for this design, the output voltage of the comparator will be connected to the analog pins of the Arduino, where it will be able to collect and process the data. For initial testing and code development, the Arduino will be powered via a USB cable, but it will later be powered via the same power supply connection on the PCB. The unused pins are left open. The RX and TX pins are used for serial communication, since the standalone signal RF generator will be connected onto the board via a USB-A connector. The schematic for the USB connector for the signal generator is displayed below in Figure 3.17. The connections for the USB-A connector is based on the connections of the breakout board by the producer of the USB RF generator, Windfreak Technologies[].

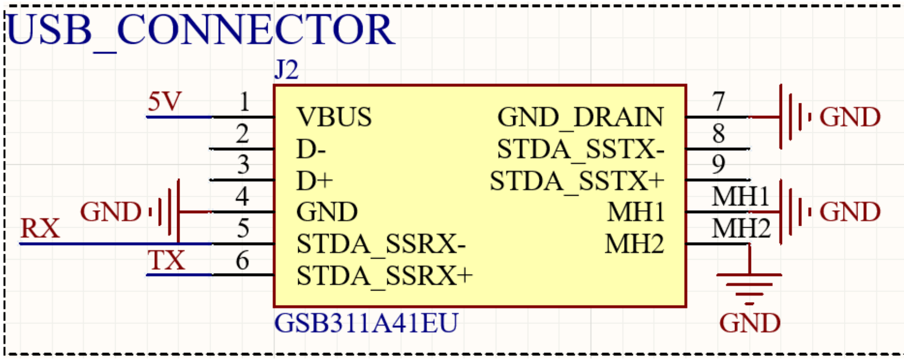

Figure 3.17: USB-A connector schematic in Altium.

The process for soldering and testing the board is the same for the second design. Instead of replicating the entire IR power sweep experiment, only the S(1,1) and S(2,1) response were measured. The PCB layout and soldered board is displayed below in Figure 3.18 and Figure 3.19, respectively. This allows the RF signal generator to be controlled by the Arduino, which will be important for future applications.

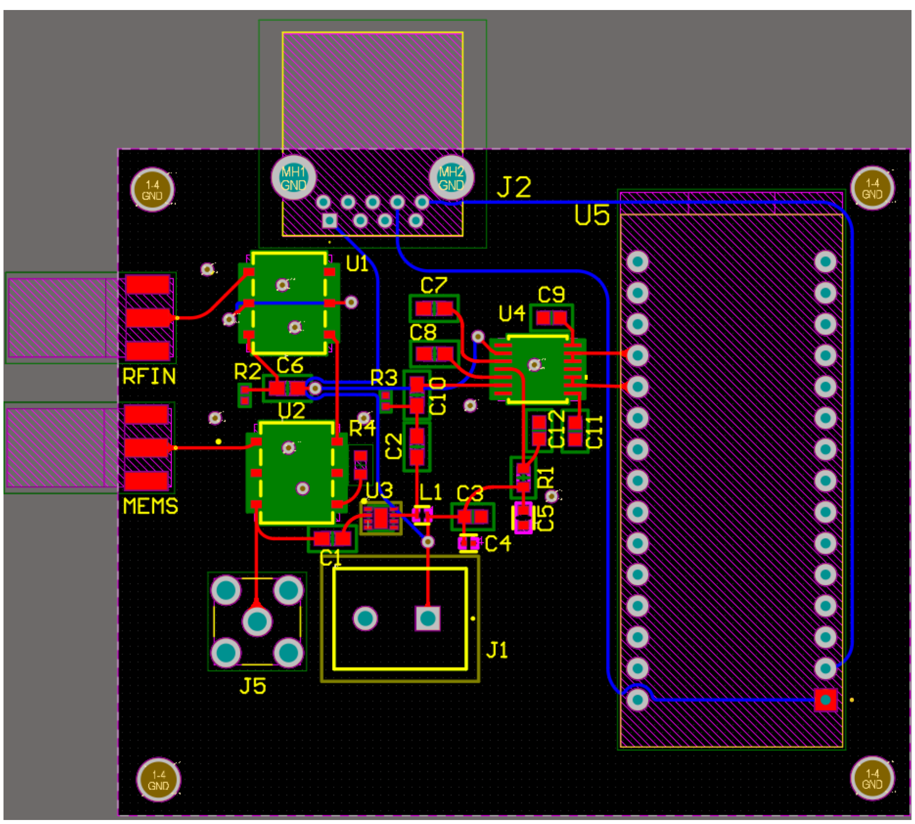

Figure 3.18: Design 2 PCB Layout (a) 2D model (b) 3D model.

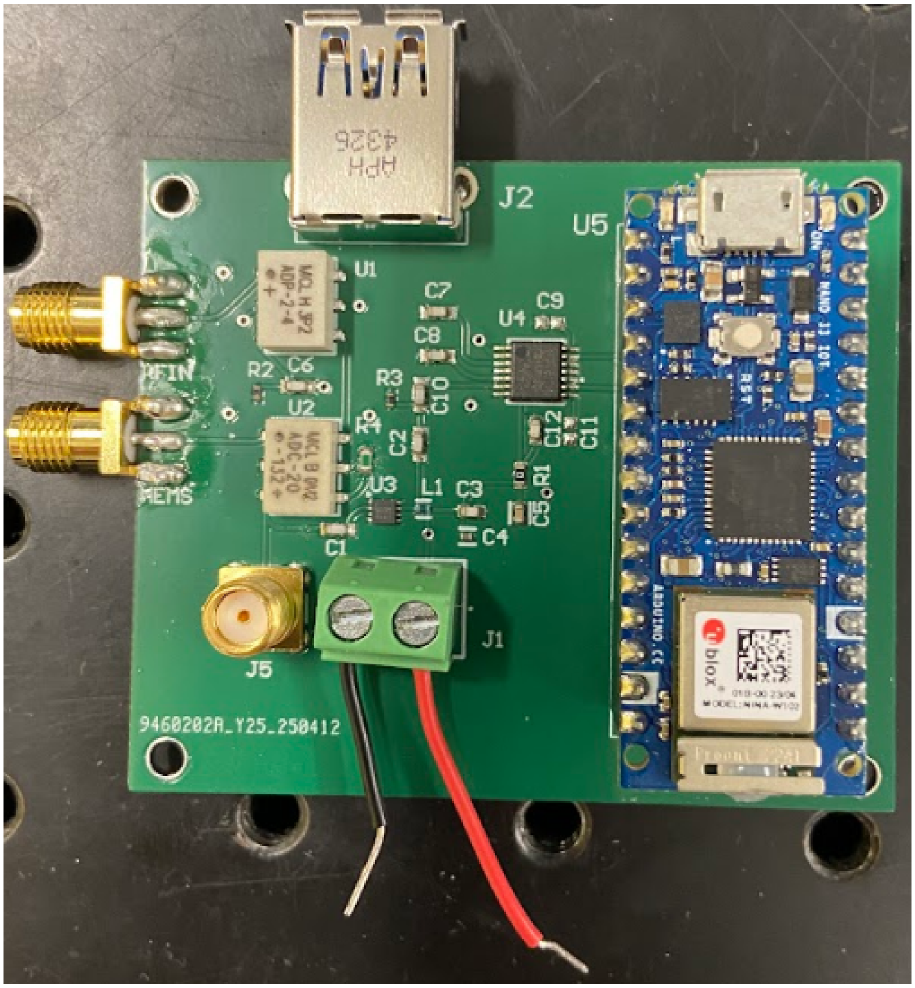

Figure 3.19: Design 2 soldered board.

To test the functionality of the Arduino, a code was developed that reads the input of the analog pins and converts it into voltage. Using a phase shifter connected to the MEMS input, it was observed that the phase voltage output changes due to the phase shift. The RF signal generator was then plugged into the PCB, and it was observed that the settings of the source could be controlled via the Arduino. The board connection and the generated signal from the USB source is depicted in Figure 3.20. Testing and code development for this design is currently still being conducted.

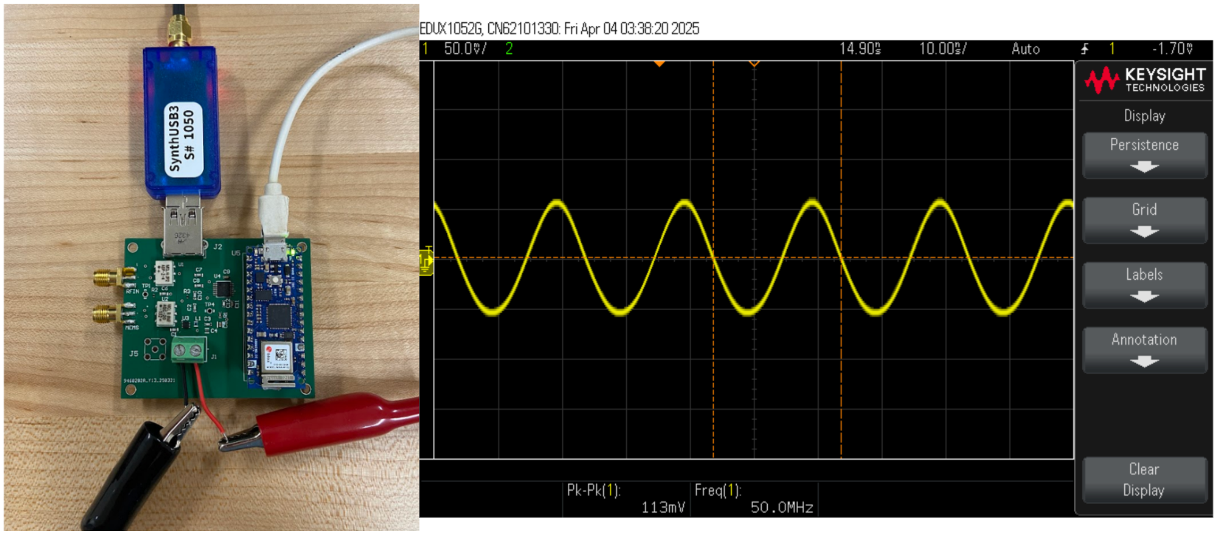

Figure 3.20: Experimental set-up & signal generated from USB RF source.

3.4 Design 3: Wire Bonding MEMS onto PCB

The goal of this design is to have a fully standalone IR detector with the Arduino to process the data and the RF signal generator as the source. This design incorporates the MEMS onto the PCB, therefore it has the area required for a diced out MEMS and includes the pads required for wire bonding. The design also incorporates the external matching network that is utilized onto the board. The matching network is an LC network with a capacitors in parallel and inductors in series for tuning. The main capacitor is a mechanical varactor used to tune the matching network. The schematic for the matching network and approximate dimensions of the pad for the MEMS is displayed in Figure 3.21

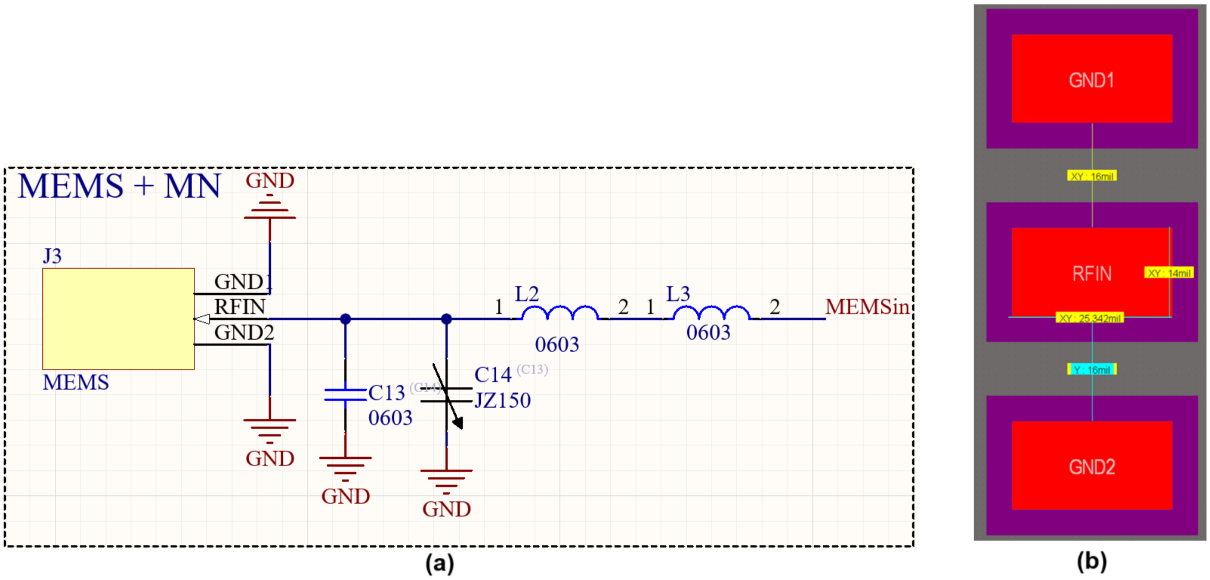

Figure 3.21: (a) MEMS input with matching network schematic (b) Dimensions of pads for wire bonding: 16 mil gap between pads, width of 25 mils, and height of 13.75 mils.

The design consists of two different versions. The first version is based on design 1, where the input and output connections are all external through SMA connectors. This version allows us to validate the system and wire bonded MEMS by connecting the signal to an oscilloscope or lock-in for testing and experiments. The second version is based on design 2, where an Arduino is used to process the data and the USB RF signal generator is the source. This design version allows the entire system to be standalone and will be the version used in the miniaturized cancer-detecting device. The PCB layout and soldered boards are displayed below in Figure 3.22 and Figure 3.23. However, development with the board and integration with the MEMS is currently still an ongoing process.

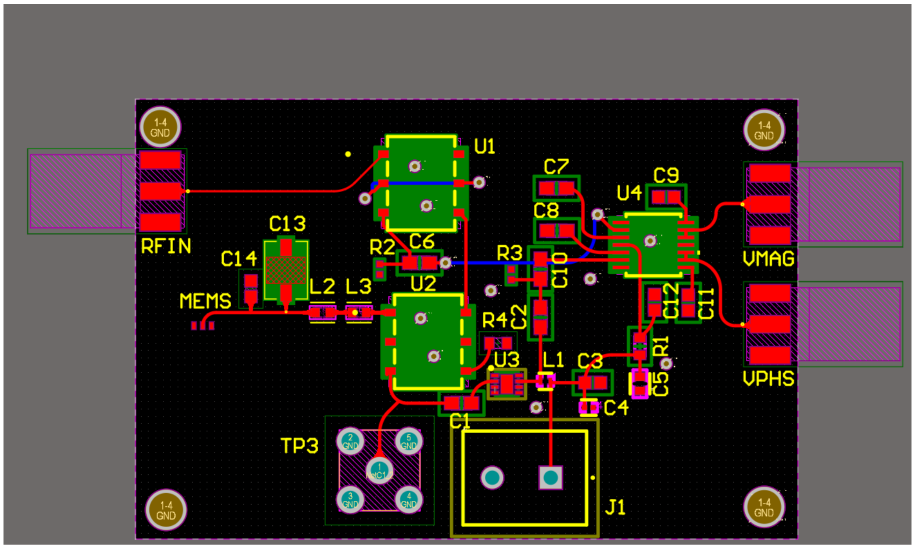

(a)

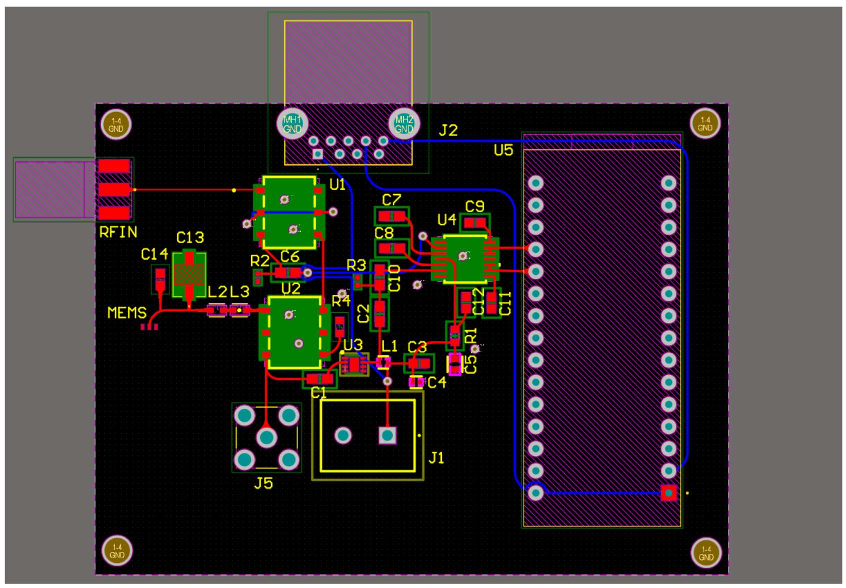

(b)

Figure 3.22: Design 3 PCB layout (a) SMA outputs version (b) Arduino & RF generator version.

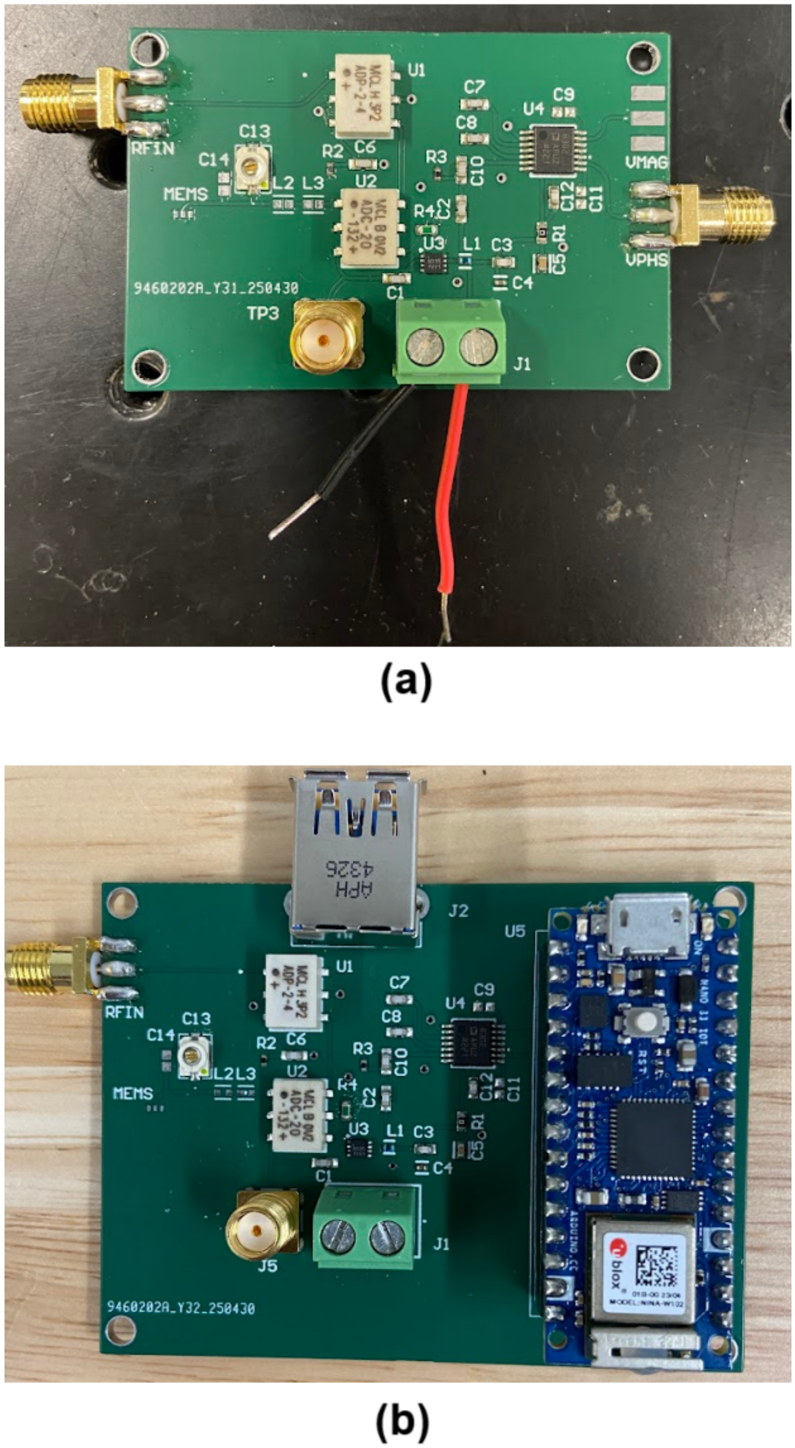

Figure 3.23: Design 3 soldered board (a) SMA outputs version (b) Arduino & RF generator version.

Chapter 4

Conclusion

4.1 Summary

ADS simulations and experimental results confirm that the designed PCBs discussed in this thesis successfully replicate the bench-top set-up and function as intended. The work presented provides the foundation needed to develop a spectroscopy IR sensing system that functions at room temperature. The first design functions as a test board and replicates an IR power sweep experiment to exhibit the functionality of the designed board. The second design is based on the first design with the addition of an Arduino for micro-processing and a standalone on-board RF signal generator. The Arduino is able to successfully process the voltage data from the RF comparator, while also controlling the RF signal generator. Lastly, the third design combines the previous designs to create a self-contained system by allowing the MEMS to be wire bonded onto the PCB. The specific use-case is a miniaturized and portable device that effectively provides spectral information for head and neck cancer. However, when further developed, this system could be utilized in a variety of fields and applications, providing a cheap and accessible alternative to IR sensors and spectroscopy systems.

4.2 Future Outlook & Next Steps

In order to fully develop the head and neck cancer detecting device, further work for this research is required. Currently, each MEMS device is selective at a small range of wavelengths. Future work for this research includes multiplexing an array of MEMS, so that it can provide spectral information over a wider wavelength range. This requires a self-calibration system where the Arduino can detect whether the MEMS is being excited at the correct resonant frequency, and if not, it would automatically control the USB RF source to change to the resonant frequency. If the resonant frequency is changed, the matching network must also be tuned to compensate for the shift. Therefore, the Arduino will also tune a matching network via controlling the reverse voltage bias of varactors. These developments are essential for the head and neck cancer detecting device, as well as future applications, since it will improve the efficacy of the cancer-detecting device if the spectral information over a wide range of wavelengths can be collected. Lastly, a 3D enclosure for the PCB and a lens to focus the IR signal incident onto the wire bonded MEMS is also expected to be developed.

References

[1] M. E. Gülseren, M. Benson, R. W. Parker, J. Segovia-Fernandez, E. T.-T. Yen, and J. S. Gómez-Díaz, "Experimental study of spectrally selective mems/metasurface infrared detectors," *IEEE Sensors Journal*, vol. 24, no. 11, pp. 17 313–17 323, 2024.

[2] Z. Lin, M. Benson, M. E. Gülseren, W. Putnam, and J. S. Gómez-Díaz, "Ultra sensitive ir detection based on metasurface-loaded mems," Poster presented at: EC-EXPO2024, UC Davis, Apr. 2024.

[3] Y. Hui, S. Kang, Z. Qian, and M. Rinaldi, "Uncooled infrared detector based on an aluminum nitride piezoelectric fishnet metasurface," *Journal of Microelectromechanical Systems*, vol. 30, no. 1, pp. 165–172, 2021.

[4] Y. Hui, J. S. Gómez-Díaz, Z. Qian, A. Alù, and R. M., "Plasmonic piezoelectric nanomechanical resonator for spectrally selective infrared sensing," *Nat. Commun.*, vol. 7, p. 11249, 2016.

[5] R. Bhan and V. Dhar, "Recent infrared detector technologies, applications, trends and development of hgcdte based cooled infrared focal plane arrays and their characterization," *Opto-Electronics Review*, vol. 27, no. 2, pp. 174–193, 2019. [Online]. Available: https://www.sciencedirect.com/science/article/pii/S1230340219300034

[6] A. Devices, "Ad8302: Lf–2.7 ghz rf/if gain and phase detector data sheet (rev.b)," Sep. 2006, available: https://www.analog.com/media/en/technical-documentation/data-sheets/ad8302.pdf.

[7] J. Larson, P. Bradley, S. Wartenberg, and R. Ruby, "Modified butterworth-van dyke circuit for fbar resonators and automated measurement system," in *2000 IEEE Ultrasonics Symposium. Proceedings. An International Symposium (Cat. No.00CH37121)*, vol. 1, 2000, pp. 863–868 vol.1.

[8] M. V. Schneider, "Microstrip lines for microwave integrated circuits," *The Bell System Technical Journal*, vol. 48, no. 5, pp. 1421–1444, 1969.

[9] H. Wheeler, "Transmission-line properties of parallel strips separated by a dielectric sheet," *IEEE Transactions on Microwave Theory and Techniques*, vol. 13, no. 2, pp. 172–185, 1965.

[10] ——, "Transmission-line properties of a strip on a dielectric sheet on a plane," *IEEE Transactions on Microwave Theory and Techniques*, vol. 25, no. 8, pp. 631–647, 1977.

[11] E. O. Hammerstad, "Equations for microstrip circuit design," in *1975 5th European Microwave Conference*, 1975, pp. 268–272.

[12] E. Hammerstad and O. Jensen, "Accurate models for microstrip computer-aided design," in *1980 IEEE MTT-S International Microwave symposium Digest*, 1980, pp. 407–409.

[13] JLCPCB. (2025) "impedance control in pcb manufacturing". Accessed: May 11, 2025. [Online]. Available: https://jlcpcb.com/impedance

[14] Loctite, "Engineering manual loctite gc 10 solder paste," Feb. 2015, available: https://www.diverseelectronics.com/upload/documents/LoctiteGC10$_EngMan.pdf$.